2013-07-05

The Effect of Carbon Additives on the Microstructure and Performance of Alkaline Battery Cathodes

Douglas Robert Nevers
Brigham Young University - Provo

BYU ScholarsArchive Citation

Nevers, Douglas Robert, "The Effect of Carbon Additives on the Microstructure and Performance of Alkaline Battery Cathodes" (2013). *All Theses and Dissertations*. 3689.
https://scholarsarchive.byu.edu/etd/3689

The Effect of Carbon Additives on the Microstructure and Performance of Alkaline Battery Cathodes

Douglas R. Nevers

A thesis submitted to the faculty of
Brigham Young University
in partial fulfillment of the requirements for the degree of

Master of Science

Dean R. Wheeler, Chair
William G. Pitt
W. Vincent Wilding

Department of Chemical Engineering

Brigham Young University

July 2013

ABSTRACT

The Effect of Carbon Additives on the Microstructure and Performance of Alkaline Battery Cathodes

Douglas R. Nevers
Department of Chemical Engineering, BYU
Master of Science

This thesis describes research to understand the relationships between materials, microstructure, transport processes, and battery performance for primary alkaline battery cathodes. Specifically, the effect of various carbon additives, with different physical properties, on electronic transport or conductivity within battery cathodes was investigated. Generally, the electronic conductivity increases with carbon additives that have higher aspect ratios, smaller particle diameters, higher surface areas, and lower bulk densities. Other favorable carbon aspects include more aggregated and elongated carbon domains which permit good particle-to-particle contacts. Of the various carbon additives investigated, graphene nanopowder was the best performer. This graphene nanopowder had the smallest particle diameter, highest surface area, and one of the lowest Scott densities of the carbon additives investigated as well as well-connected, interspersed carbon pathways. Notably, a typical effective ionic conductivity is more than 50 times less than the electronic conductivity (5.7 S/m to 300 S/m, respectively) for a high-performance cathode. Thus, alkaline battery cathodes could be redesigned to improve ionic conductivity for optimal performance. This work expanded on previously published work by relating additional carbon-additive material properties–specifically, particle morphology, surface area and Scott density–and their corresponding cathode microstructure to the fundamental transport processes in alkaline battery cathodes.

Keywords: electronic conductivity, porosity, alkaline battery, cathode microstructure

ACKNOWLEDGMENTS

I would like to acknowledge Dr. Wheeler and Dr. Pitt for insightful suggestions and thoughtful discussions, Yuan Wen for completing the SEM/FIB imaging shown here, and my family for support and encouragement.

Contents

List of Tables

List of Figures

List of Symbols

Roman

A	cross-sectional area
b	Bruggeman-fitting parameter
D	intrinsic diffusivity of the electrolyte
D^{eff}	effective diffusivity of the electrolyte
d_{90}	90% of particle diameters (or distributions) are below this value
E	Young's modulus
h	height
h_{c}	current spreading length
K_o	coefficient of earth pressure at rest
l_o	thickness of nylon sleeve
m	mass
P	pressure
r	radius
Δr	change in cathode radius
R_{app}	resistance of the apparatus

R_c	contact resistance
R_cathode	resistance of the cathode sample
R_R	resistance of the external resistor
R^2	coefficient of determination
V_app	voltage drop over apparatus
V_R	voltage drop over the external resistor

Greek

ϵ	porosity
ϵ_inter	inter-particle porosity
ϵ_r	radial strain
ϵ_tot	overall porosity
κ	intrinsic ionic conductivity
κ^eff	effective ionic conductivity
ρ_p	weighted-particle density
ρ_s	weighted-skeletal density
σ_eff	effective electronic conductivity
σ_o	Bruggeman-fitting parameter, maximum electronic conductivity
σ_r	radial stress
σ_z	axial stress
τ	tortuosity

Chapter 1

Introduction

1.1 Motivation

Both mature and emerging battery technologies require further improvements to meet future demands. These demands include higher energy at lower cost, and improved safety, especially in larger systems [1]. An important aspect in improving overall battery performance is refining the electrode microstructure to enhance the fundamental transport processes (ionic and electronic) that have a strong effect on battery performance [2, 3]. This is especially important for high-drain or rapid-discharge applications (such as personal electronics) that require rapid electron and ion transport. Improved understanding of the material-microstructure-transport relationships that are fundamental to battery performance will, potentially, lead to higher energy, lower cost, more reliable, and longer-lasting batteries.

This work focuses on primary alkaline (MnO_2/Zn) batteries. Unfortunately, the redox active material in these batteries is not highly electronically conductive, but rather only semi-conducting; thus, a redox inactive conducting material such as a conductive carbon must be added to improve the electronic transport process and enable successful battery performance. Nevertheless, the addition of these conductive additives directly reduces the available volume for active energy storage. Hence, volumetrically efficient conductive additives are essential to maximize energy storage as well as electronic conductivity. Various conductive carbon additives have been used in batteries, including carbon black, graphite, carbon fibers, and carbon nanotubes [4–11]. Despite the importance and variety of conductive additives, alkaline batteries have not received substantial investigation into the effect of different carbon additives on battery performance [3, 9, 12–14]. The lack of understanding of the effect of different carbon additives, their volumetric efficiencies, and their transport characteristics for alkaline (MnO_2/Zn) batteries motivates this research.

1.2 Scope of work

This thesis describes research that fills a crucial need to understand the relationship between materials, microstructure, transport processes, and battery performance. Specifically, this work focuses on carbon additives in primary alkaline batteries.

The chief objective of this work is to determine the effect of various carbon additives on electronic transport or conductivity within battery cathodes. Specifically, this research investigates the effect on electronic conductivity of carbon additives with different physical properties such as particle size and morphology. This work also attempts to determine the effect of the underlying cathode microstructure on electronic conductivity. Nevertheless, improvements in electronic transport need to be achieved without significantly impairing other desirable design features such as manufacturability and ionic transport.

To accomplish these objectives, two experimental apparatuses were developed: one that enables simultaneous measurement of porosity and electronic conductivity, and another that measures ionic conductivity. The cathode microstructure was varied by using different carbon additives with various morphologies and particle sizes and compressing the sample to various porosities. To relate the electronic conductivity performance to the cathode microstructure, the microstructure was imaged using SEM/FIB (scanning electron microscopy/focused-ion beam). Additionally, the electronic conductivity data for the various cathodes investigated were compared to the physical properties of the carbon additives that they contain. Ultimately, this research provides understanding that paves the way for design and performance improvements for alkaline batteries.

1.3 Outline

The remainder of this document is organized as follows.

Background. Chapter 2 is a brief description of alkaline batteries, 2) conductive carbon additive characteristics, and 3) previously observed relationships between materials, microstructure, transport processes and battery performance.

Alkaline battery. Chapter 3 reports experimental electronic conductivities for various carbon additives at both compressed and relaxed conditions. Additionally, the electronic conductivity for the various carbon additives are related to their respective material properties and cathode microstructures. The ionic conductivity for one carbon additive is also reported. Finally, conclusions on this work as well as possible future work are presented.

Chapter 2
Background

This work requires a foundational understanding of alkaline battery chemistry, and the relationships between materials, microstructure, transport processes, and battery performance. One must also understand the characteristics of the different types of conductive carbon additives, and how different carbon additives can contribute to improved battery performance.

2.1 Alkaline battery chemistry

Alkaline batteries are typically used in portable electronics (i.e. AA, C, and D cell batteries). Based on an estimate of the battery market in 2003, alkaline batteries are the largest primary battery system (US \$10 billion) and make up about a fourth of the overall battery market [3]. Alkaline batteries are constructed using electrolytic manganese dioxide (EMD) as the cathode, zinc powder as the anode, and aqueous KOH as the electrolyte (approx. 9 M) [15]. EMD is predominately composed of short-range-ordered $\gamma-\mathrm{MnO_2}$, and contains only a small fraction (4-9 wt%) of graphite that is added to improve the electronic conductivity [15, 16]. During discharge, the $\mathrm{MnO_2}$ is reduced while Zn is oxidized (see Eqn. 2.1,2.2) .

$$\mathrm{2MnO_2 + H_2O + 2e^- \rightarrow Mn_2O_3 + 2OH^-}\,, \tag{2.1}$$

$$\mathrm{Zn + 2OH^- \rightarrow ZnO + H_2O + 2e^-}\,. \tag{2.2}$$

2.2 Relationships between materials, microstructure, transport processes and battery performance

2.2.1 Material and microstructural origins of transport processes

Battery performance is partially controlled by electronic and ionic transport processes [3]. These processes can either be facilitated or hindered by the microstructure of the electrode [17]. Electronic transport is essential to access and utilize the electrons, which during discharge are liberated in the anode and consumed in the cathode. Electronic transport is facilitated by the addition of conductive carbon to form electronically conductive pathways within the electrode, since redox active materials are typically electrical insulators or semiconductors. In addition, ionic transport is essential to maintain charge conservation after the redox reaction changes the oxidation state of the active material. Ionic transport is facilitated by the porosity of the electrode that permits reservoirs and pathways for the electrolyte. Figure 2.1 illustrates the relationship between the physical carbon and pore structures and the electronic and ionic transport pathways within an electrode.

To ensure the maximum utilization of the active material, the ionic and electronic transport processes need to be promoted throughout the electrode. This requires that the pores and conductive carbon be dispersed throughout the electrode to minimize the transport distance for the ions and the electrons, respectively [6, 18, 19]. In addition, electrodes are made of small particles to minimize transport distances, maximize surface area for redox reactions, and efficiently use the electrode volume. Implicit in the concept of electronic and ionic pathways is the understanding that conductivity is better viewed as a volumetric rather than gravimetric property, which again accents the need for volumetrically efficient conductive additives.

The nature of the electronic and ionic transport pathways can be described by percolation theory. In the case of electronic conductivity, percolation theory indicates that a composition threshold exists above which the conductivity will increase to that of the conductive additive,

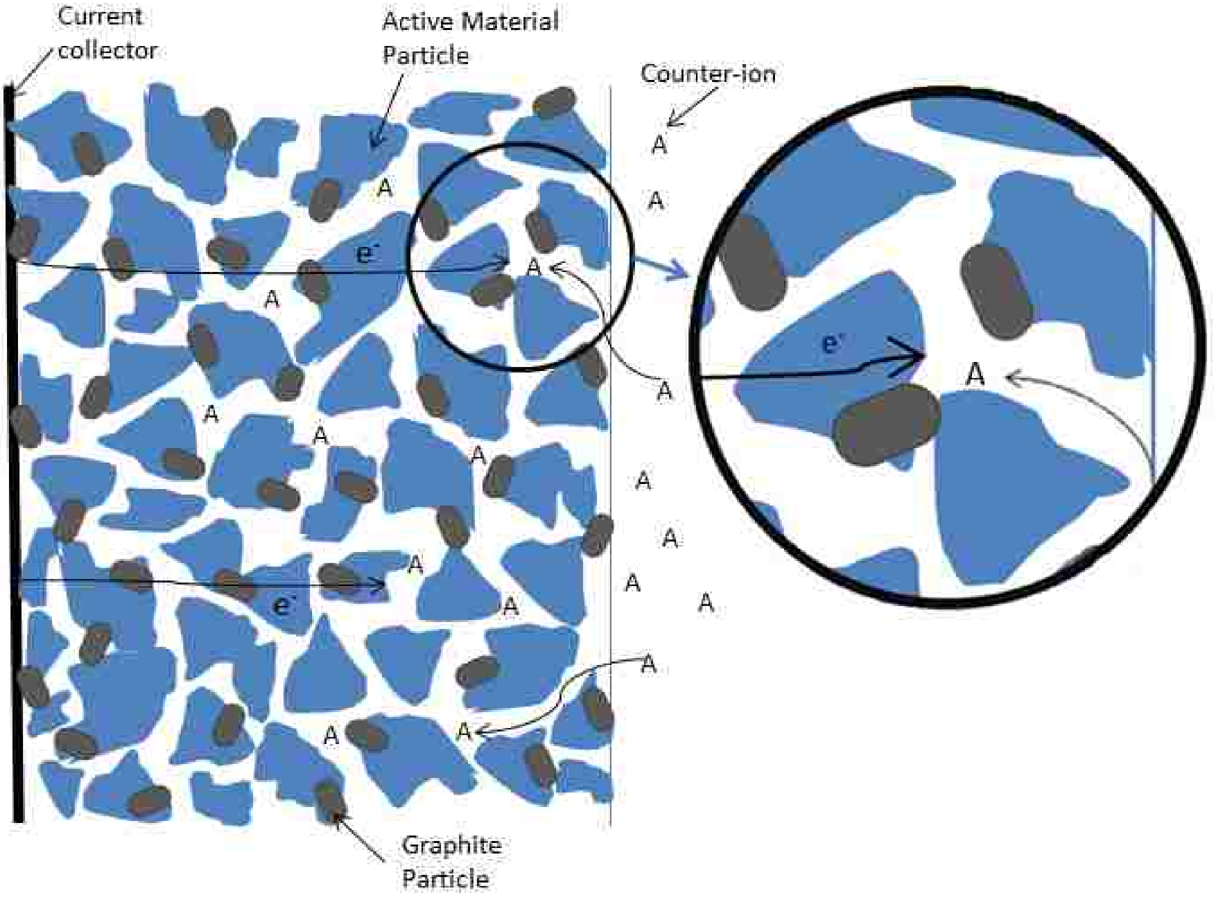

Figure 2.1: Schematic of a representative porous electrode, illustrating the relationship between microstructure and transport pathways.

but below which the electrode will have conductivity values that are more similar to the background matrix (active material and pores) [7, 20–23]. Below the percolation threshold the transport pathways do not completely transverse the electrode and are limited by the low conductivity of the redox active material. In the case of this work, the volume fraction of the carbon within the cathode is approximately 7 vol%. This carbon volume fraction is below the percolation threshold for spherical particles (29 vol%) and near that of rod-like particles (5 vol%), suggesting that alkaline battery cathodes are below the carbon percolation threshold [24, 25]. Figure 2.1 illustrates a case in which carbon-only pathways are below the percolation threshold. Thus, the presence of carbon additives enhances the electronic conductivity of the cathode, but not to the degree of a percolated carbon network.

2.2.2 Influences of material characteristics

Numerous parameters affect the transport processes and microstructure including the conductive carbon type, shape, size, and amount as well as the electrode porosity, degree of compression, mixing, and thickness [10, 12, 26]. For instance carbon characteristics such as purity, surface area, and crystallinity affect the overall electrode characteristics [8]. Furthermore, there is a substantial interplay between the many different material characteristics, which ultimately determine the microstructure, transport, and performance of a battery electrode. For example, a carbon additive with a high aspect ratio is more efficient in transporting electrons and hence often requires a lower percentage of the electrode composition compared to a lower-aspect-ratio carbon [27, 28].

2.2.3 Conductive carbon

Carbon additives. Various types of carbon additives are used as conductive additives in battery electrodes. Namely, carbon black, graphite, carbon fibers or filaments, carbon nanotubes, and blends such as graphite and carbon black mixtures. Alkaline batteries typically use graphite [9, 12, 26].

The effect of different conductive carbon additives has been substantially investigated for lithium-ion electrodes [18, 20, 28–47]. However, MnO_2 (EMD) cathodes have not received nearly as much research attention despite their larger market size [3, 9, 12, 48–50]. The lack of research on the effect of different carbon additives and their characteristics for alkaline batteries motivates this work.

Carbon characteristics. Carbon black and graphite are the most common carbon additives in commercial batteries because they have good conductivity and are inexpensive. Carbon fibers and nanotubes are used less often, despite providing excellent conductivity in addition to long-range connectivity due to their high aspect ratio, because they are expensive, hard to mix, and can lead to shorting across the separator [8, 15, 32]. Graphite is inexpensive, mechanically strong, lubricating, and corrosive-resistant in addition to having a higher bulk

Table 2.1: Conductivities and mobilities of graphite along and perpendicular to the atomic plane at 300 K [9]

Direction	Conductivity ($\mathrm{S\,cm^{-1}}$)	Mobilities ($\mathrm{cm^2\,V^{-1}\,s^{-1}}$)
Along the plane	2.26×10^4	1.25×10^4
Perpendicular to the plane	5.9	3.3

conductivity than carbon black [15]. These advantages as well as it being the standard conductive additive for commercial alkaline batteries motivate this work's focus on graphite.

D.D.L. Chung reviewed graphite, its characteristics, and applications. Graphite is a crystalline and anisotropic material that conducts well along its layers or planes, but conducts poorly perpendicular to its plane layers [9]. Graphite is composed of layers of sp^2-hybridized graphene sheets. The layers are held together by van der Waals forces. Graphite can be a single crystal or polycrystalline [9]. Its electronic conductivities and mobilities along the atomic plane (a-axis) and perpendicular to that plane (c-axis) are reported in the Table 2.1.

Expanded Graphite. Another type of graphite is expanded graphite, which is expanded along the c-axis, perpendicular to the graphene planes. Expanded graphite is usually only partially exfoliated, since the graphene (individual graphite sheets) are not completely separated from one another as in neat graphene [51, 52]. Exfoliation increases the electronic resistivity–as much as two orders-of-magnitude–along the graphene sheets (a-axis) due to bending in the sheet, but decreases the resistivity in the direction perpendicular to the graphene planes (c-axis) due to the bending. Thus, exfoliation produces an anisotropic trade-off in conductivity values. This trade-off suggests the possibility of an optimal degree of exfoliation and/or more broadly an optimum ratio for mixture of graphites with different degrees of expansion or exfoliation to optimize transport and battery performance. Additionally, exfoliated graphite has been used as an adsorbent for gas chromatography and as a sorbent for heavy oil [52–54]. This indicates the potential for electrolyte adsorption within expanded graphite that may improve ionic transport pathways. This work on different graphites morphologies will provide preliminary results about this trade-off, and direct future research on the effect of graphite exfoliation on battery performance.

2.2.4 Microstructural design affects performance: graphite morphology and particle size

Commercial graphite morphologies. TIMCAL is a well-known supplier of graphite products for conductivity enhancement. They report three main graphite grades (morphologies): small crystal agglomerate (e.g TIMCAL KS-15), flake graphite with anisotropic character (non-expanded) (e.g. TIMCAL MX-15), and expanded graphite (TIMCAL BNB90) [55]. TIMCAL indicates that expanded graphite is used for premium AAA-AA alkaline batteries (TIMCAL BNB90) while natural or synthetic graphite is used for value batteries (TIMCAL KS-15) [15]. In addition, completely exfoliated graphite, or graphene, also produces extremely favorable electronic transport performance [13, 14]. Several carbon additives in these grades were investigated in addition to graphene and one mixture: 10 wt% fiber/90 wt% MX-15. The fibers were mixed with a large fraction of graphite to form pellets for analysis, since a 50/50 wt% mixture of graphite and fiber did not hold together. The variety of carbon additives investigated provides adequate information to accurately elucidate the effect of particle diameter, shape, bulk density, and surface area on electronic conductivity. Furthermore, different carbon morphologies may create different microstructural effects such as the dispersion of carbon throughout the electrode. Kinoshita indicates that for composites, the conductivity is controlled by the distance between carbon particles along with the number of particle-to-particle contacts [7]. The microstructural imaging and analysis allows evaluations of these effects.

Particle Size. Urfer et al. studied the effect on performance of graphite and EMD particle sizes, with and without blending carbon black, and at different discharge rates [12]. They indicate that performance mainly depends on the graphite-to-EMD ratio, the amount of

EMD in the electrode, the compression pressure, and the electrolyte conductivity. They cited a previous study that indicates the optimum performance was in the range between 0.08 and 0.10 for the graphite/EMD ratio (assuming only graphite and EMD, then the graphite composition is 7.4-9.1%), 3.05-3.10 $\mathrm{g\,cm^{-3}}$ for the cathode density, and 1.5-3 English $\mathrm{ton\,cm^{-2}}$ (133-267 MPa) for continuous compacting pressure [12].

In addition, Urfer et al. focused on the effect of EMD and graphite particle size and cathode thickness on battery performance. Numerous variables were investigated, namely graphite particle sizes, graphite amount, cathode thickness, EMD particle size, and the amount carbon black mixed with the graphite [12]. Urfer et al. reported that higher graphite content and finer particle size produced better performance, even in thicker cathodes. Additionally, thicker cathodes had a 10-15 mV higher average open-circuit voltage. However when carbon black is mixed with graphite, it reduced the EMD more than graphite due to its larger surface area, which ultimately decreases the open-circuit potential. Nevertheless, carbon black with its larger surface area has the advantage of delaying the impact of an insulating reaction product, $\mathrm{Mn(OH)_2}$, that impairs electronic transport near the end-of-battery life (or greater depths of discharge) [12]. Hence, Urfer et al. indicates that carbon black is better for low power situations while graphite is better and more commonly used in commercial alkaline battery, which face a wide range of discharge demands. In summary, this study indicates again the advantage of graphite over carbon black, and that finer graphite particles provide better electronic performance. This work builds upon the study by Urfer et al. and further investigates the effect of particle size, but with the additional variable of graphite morphology for EMD cathodes.

2.3 Conclusion

This work attempts to clarify the effect of different graphite morphologies and particle sizes on the cathode microstructure, transport processes, and thus battery performance for alkaline battery cathodes. While transport measurements have been previously performed in the case of EMD cathodes, this work adds to the discussion by providing analysis of different graphite morphologies and particle sizes as well as microstructural analysis. In general, this work seeks to generate understanding and insight into the relationships between material characteristics, microstructural properties, transport processes, and thus battery performance for this electrochemical system.

Chapter 3

Alkaline batteries

3.1 Introduction

As the previous chapter indicated, different graphite morphologies and particle sizes (materials) have diverse effects on the electrode microstructure, transport processes, and thus overall battery performance. To determine the impact on battery performance of different carbon additives and their corresponding cathode microstructures, direct electronic conductivity measurements were performed at various porosities. Testing at multiple porosities provides a means to elucidate the interplay between ionic and electronic transport processes and pathways. Specifically, the electronic conductivities are directly measured for seven different carbon-additives-based EMD cathodes, and ionic conductivity is directly measured for one carbon-additive-based EMD cathode. For instance, for a given cathode construction (i.e. materials and microstructure), there will be prescribed electronic conductivity. Ultimately, the measurement of transport properties provides a metric to relate or link the effects of various materials and cathode microstructures to battery performance.

This chapter dicusses experiments directed at quantifying and relating electronic and ionic transport processes, and thus battery performance, to their underlying material and microstructural foundations for primary alkaline batteries. Thus, the sections progress from material preparation and characterization (Section 3.2) to transport processes (Section 3.3), and finally compares the two conductivities to the corresponding cathode microstructure

(Section 3.4). Connecting the effects of different carbon additives to their impact on microstructure and performance provides insight to improve material selection and cathode design.

3.2 Material preparation

The physical properties of the carbon additives and EMD materials were obtained from manufacturers' data sheets, and as necessary from direct measurement and SEM/FIB imaging. The physical properties of interest include porosity, solid and bulk densities, surface area, particle size and morphology (see Table 3.1). An accurate understanding of the electrode material properties enables insightful understanding into their effects on battery performance.

The sample cathodes used for the dry electronic conductivity (meaning without electrolyte) measurement were prepared as follows. EMD (Tronox) and one of the carbon additives specified in Table 3.1 were weighed. The cathode composition was held constant throughout this study at approximately 95 wt% EMD and 5 wt% carbon additive. All powders were gently mixed together with a rod, except for the cathodes containing graphene and fiber/MX-15, which were mixed more vigorously (with mortar and pestle) in order to break up aggregates. All cathode powders were mixed for approximately 1 minute per gram of material. Then, two to four experimental runs were performed for each carbon type to ensure repeatable results.

As mentioned in Chapter 2, various graphite additives (i.e. small crystal agglomerate, flake, and expanded graphite) were investigated in addition to graphene and one mixture: 10 wt% fiber/90 wt% MX-15. Some characteristic physical properties for each of the investigated carbon additives are provided in Table 3.1. The property values are from the respective manufacturers' data sheets. The variety of carbon additives investigated provides adequate information to accurately elucidate the effect of particle diameter and morphology (i.e. shape) along with bulk or Scott density and surface area on electronic conductivity.

Table 3.1: Physical properties of the various carbon additives investigated

Carbon Additive	d_{90} (μm)	Shape	Scott Density ($\mathrm{g\,cm^{-3}}$)	BET Surface Area ($\mathrm{m^2 g^{-1}}$)
TIMCAL BNB90 [55]	85	strongly anisometric flakes 2-dimensional, expanded	0.03	28.4
TIMCAL MX-15 [55]	17	strongly anisometric flakes	0.065	9.5
TIMCAL SFG-6 [55]	6.5	strongly anisometric flakes	0.07	17
TIMCAL KS-15 [55]	17	isometric, irregular spheroids	0.1	12
TIMCAL KS-6 (C-NERGY KS 6 L) [55]	6.5	isometric, irregular spheroids	0.07	20
Graphene Supermarket Graphene (30-50 monolayers) [56]	4.5	12-nm thick, 4.5-μm wide	0.04^b	80
Pyrograf Nanofibers(PR-19-XT-LHT)/ TIMCAL MX-15 (10/90 wt%)^c [55, 57]		fiber (50-200 μm length, dia. 150 nm)/strongly anisometric flakes	0.049	13.25^d

[a] d_{90}means that 90% of particle diameters (or the distribution) are below the reported value.
[b] This is an approximate value based on a crude bulk density experiment.
[c] The values for carbon mixture are the weighted-averaged of the pure carbon values.
[d] The fiber surface area (17 $m^2\,g^{-1}$) is based on N_2 surface analysis.

3.3 Transport measurements

3.3.1 Electronic transport or conductivity

Conductivity apparatus. To measure the electronic conductivity of the various EMD-cathodes at various porosities, the following apparatus was developed. The apparatus is depicted in Figure 3.1a. A small stainless steel rod was inserted into the hollow nylon sleeve that was located inside a larger stainless steel tube. Then, a sample was added into the apparatus. Next, another small stainless steel rod was inserted into the top of the apparatus as far as possible. Then, a copper wire was connected to each small rod with 1/2-in. hose clamps to create two leads. This apparatus was then placed in an MTS servo hydraulic load frame (with frame load model 312.41, and controller model 8800) to compress the sample, and thus change its porosity.

To secure the apparatus and prevent electronic conductivity through the MTS instrument, the two small rods were set into metal feet or holders with parafilm between each holder and the MTS instrument. The apparatus was also held with a clamp to make sure it remained vertical even at relaxed or reduced pressure conditions. Then, the copper-wire leads were connected to a power supply according to the circuit shown in Figure 3.1b. The voltage drop was measured over both the 10.3-Ω resistor and apparatus, enabling calculation of the circuit current and the resistance of the apparatus, respectively. A National Instruments eDAQ-9215 was used to simultaneously measure and recorded the position, the applied force, and the voltage drop over the 10.3-Ω resistor and the apparatus.

The samples were compressed to approximately 20% overall porosity (4% inter-particle porosity). The change in height of the sample can be directly correlated to the change in overall porosity, using the following equation:

$$\epsilon_{\mathrm{tot}} = 1 - \frac{m}{\rho_s \pi r^2 h}\,, \tag{3.1}$$

where ϵ_{tot} is the overall porosity, m is the mass of the sample, ρ_s is the weighted-skeletal density of the sample, r is the inter-radius of nylon sleeve or of the cathode pellet, and h is the height of the cathode. (Note: the skeletal density and other density definitions are discussed in Section 3.4.) The height of the sample was determined by subtracting the height of the two rods (or effectively the height of the apparatus without the sample) from the height of the apparatus with the sample. The height was measured with great precision ($\pm 2.54\ \mu m$), using a Height Master Gage (Pacific Gage Co.).

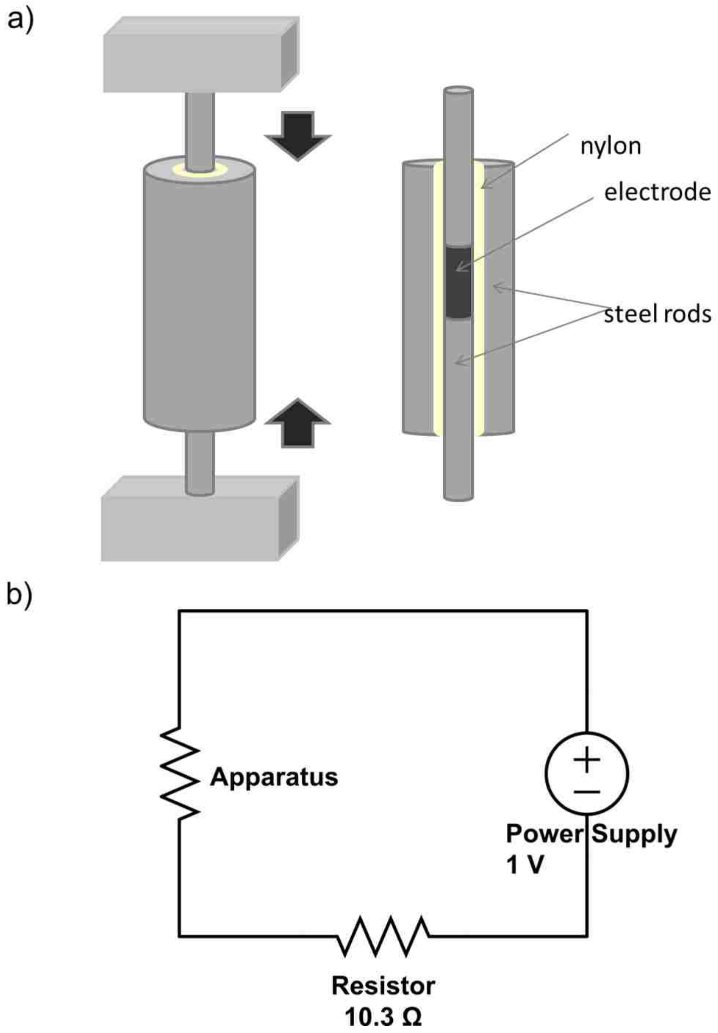

Figure 3.1: Schematic of the (a) electronic conductivity apparatus along with its place within (b) the circuit used to perform the conductivity measurements.

The electronic conductivity was measured both under active compression (i.e. still under pressure after the porosity had changed), and at a relaxed condition (with the pressure removed). To not only determine the electronic conductivity as various porosity but also at a relaxed state rather than only under active compression, the following procedure was followed. The sample was

1. compressed to reduce the starting height by 0.254 cm (0.0254-cm/s rate),

2. held at a constant position or height for 30 s, allowing for mechanical equilibrium to be achieved,
3. relaxed by reducing the pressure with a 0.127-cm step back (0.0127-cm/s rate),
4. held at a constant position at the reduced-pressure for 20 s, and
5. re-compressed by 0.127 cm to the position or height (in step 2) in preparation to repeat this sequence starting at step 1.

This process was repeated until the overall porosity was around 20%. The points used from the compressed and relaxed conditions were the following: the last point from the first compression step (i.e. end of step 2), which was most likely to be mechanically relaxed, and the last point of the relaxed state (i.e. end of step 4), respectively. Finally, the end height of the sample was measured to verify that the physically measured change in height agreed with that reported by the MTS instrument/DAQ system. Also, the apparatus was cleaned between each different carbon additive by passing several stripes of paper through the nylon rod until there was minimal carbon residue on a stripe of paper that had passed through the apparatus.

Contact resistance. The contact resistance of the apparatus was determined to ensure accurate electronic conductivity measurements of the cathode samples. Two main sources of contact resistance were investigated, namely contact resistance of the metal apparatus (i.e. leads, small rods) and the contact resistance of the metal rods and the cathode sample.

The contact resistance of the metal apparatus, due to the connections between the two copper leads and two small rods, was determined by compressing the small steel rods together within the apparatus without an electrode sample between them. Above a pressure of 2 MPa, the apparatus contact resistance was negligible (less than 0.1 Ω). (Note: for the MTS instrument, force uncertainty was approximately 44.5 N, which corresponds to 1.4 MPa for the cross-sectional area used in these experiments). In addition, the pressure for the relaxed condition data points is generally above 2 MPa.

To determine the contact resistance between the small steel rods and the cathode sample, a thin-film cathode experiment was performed for select carbon-additive-based cathodes. The contact resistance between the rods and the cathode sample (R_c) is described by the following equation:

$$\begin{aligned} R_\mathrm{app} &= R_\mathrm{cathode} + R_\mathrm{c} \\ &= \frac{1}{\sigma_\mathrm{eff} A}\left(h + h_\mathrm{c}\right), \end{aligned} \tag{3.2}$$

where R_app is the resistance of the apparatus, R_cathode is the resistance of the cathode, σ_eff is the effective electronic conductivity of the sample, A is the cross-sectional area of the cathode, h is the height of the cathode, and h_c is the height equivalent for the additional resistance due to poor contact between the metal rods and the sample. The height equivalent of the contact resistance is analogous to the entrance length of fluid flow in a pipe, and physically accounts for the spreading of the current from the few contact points or junctions between the stainless steel rods and the cathode sample [58]. Figure 3.2 illustrates that the current spreads out from the few points of contact between the rod and the cathode sample, and after a certain spreading, or entrance, length the current streamlines have become essentially parallel and uniform.

Typically, the normal conductivity measurements were performed with cathode heights that were approximately 2 cm. To more accurately determine h_c, the thin-film cathode sample heights need to be as small as possible to minimize R_cathode (based on Equation 3.2). Thin-film samples of approximately 0.1 cm were used determined h_c, since smaller samples produced significant resistance variations. A modified compression procedure from the one described above for the conductivity measurements was used. Essentially, the steps and rates were scaled down by one order of magnitude, and the relaxation steps were performed in ten smaller incremental steps until the original height before the latest compression step was reached. The incremental relaxation steps were to ensure that a relaxed condition

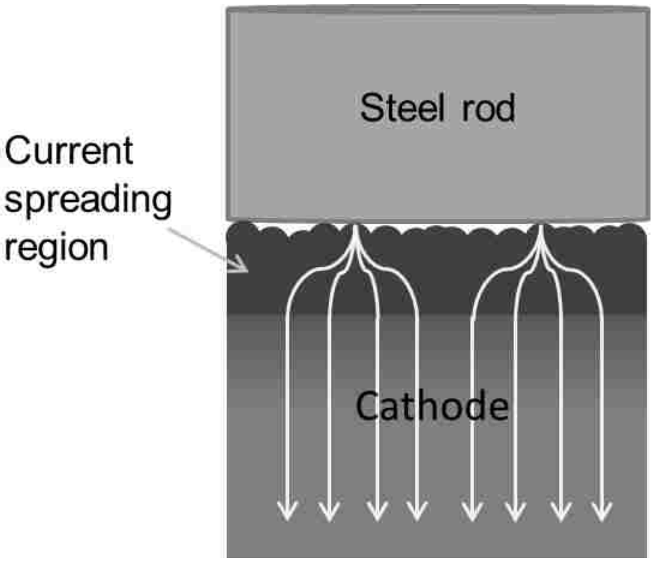

Figure 3.2: Schematic of the current spreading region from contact junctions to bulk sample.

measurement was obtained for each compressed condition point. Specifically, the procedure for thin cathode samples was as follows. The sample was

1. compressed to reduce the starting height by 0.0254 cm (0.00254-cm/s rate),
2. held at a constant position or height for 30 s, allowing for mechanical equilibrium to be achieved,
3. relaxed by reducing the pressure in a series of incremental steps back to ensure that relaxed, or low-pressure, conditions was achieved, specifically,
    (a) reduced pressure with a 0.00254-cm step back (0.000254-cm/s rate),
    (b) held at a constant position for 10 s,
    (c) repeated steps 3a and 3b until original height (before step 1) was reached,
4. re-compressed by 0.0254 cm to the position or height (in step 2) in preparation to repeat this sequence starting at step 1.

The points used from the compressed and relaxed states for the thin-film cathode experiments were the following: the last point from the first compression step (i.e. end of step 2), which was most likely to be mechanically relaxed, and the first data point from the relation step at a low pressure (1-2 MPa) (during step 3b). The height, at which these low-pressure, or relaxed, data points were obtained, within the series of incremental relaxation steps, increased as the cathode sample become more compressed, since more steps were required to reduce the additional compressing pressure.

Rather than perform this experiment for each of the carbon additives, two representative carbon samples were selected: one with a relatively high electronic conductivity (TIMCAL BNB90) and one with a relatively low electronic conductivity (TIMCAL KS-15). These selections should describe the extremes of the dependence of h_c on σ_eff. Figure 3.3 shows a plot of the resistance vs. height for both thick and thin cathode sample data at several pressures for KS-15 and BNB90. The almost two order-of-magnitude difference in the resistance between BNB90 and KS-15 for the thicker samples validates the selection of these materials as the respective high and low conductivity additives.

Table 3.2 reports the slope and intercept of the constant-pressure fits depicted in Figure 3.3 for KS-15 and BNB90. The electronic conductivity data was fit using linear least-squares regression analysis. The fitting equation used to generate the fitting curves is the second line of Equation 3.2. Because the two fitting parameters (h_c and $\sigma_\mathrm{eff} A$) differ from the usual slope and y-intercept, York's method was used to obtain the least squares fit [59]. The quality of the fit was determined using coefficients of determination (R^2). A R^2 value of 1 indicates an exact fit. For these correlations, the mean R^2 value is 0.98 and the lowest value is 0.92, indicating reasonably good fits. The correlation for KS-15 at 2 MPa (see Table 3.2) was not used because the y-intercept was negative, which is not physically realistic. This is most likely due to insufficient data for thin samples, and thus significant extrapolation from the thick sample values.

Table 3.2: Parameter values for resistance vs. cathode height correlations at various pressures. The value in parentheses was not used in subsequent analysis as explained in the text.

Carbon Additive	P (MPa)	slope (Ω/cm)	R_c (Ω)	h_c (cm)
BNB90	16.7	4.5	1.08	0.241
	31.5	2.8	0.51	0.185
	72.5	1.7	0.43	0.252
KS-15	2.3	47.6	-465.8	(-0.978)
	19.5	25.6	4.92	0.192
	56.8	9.7	2.08	0.215
	14.2	3.3	0.88	0.272

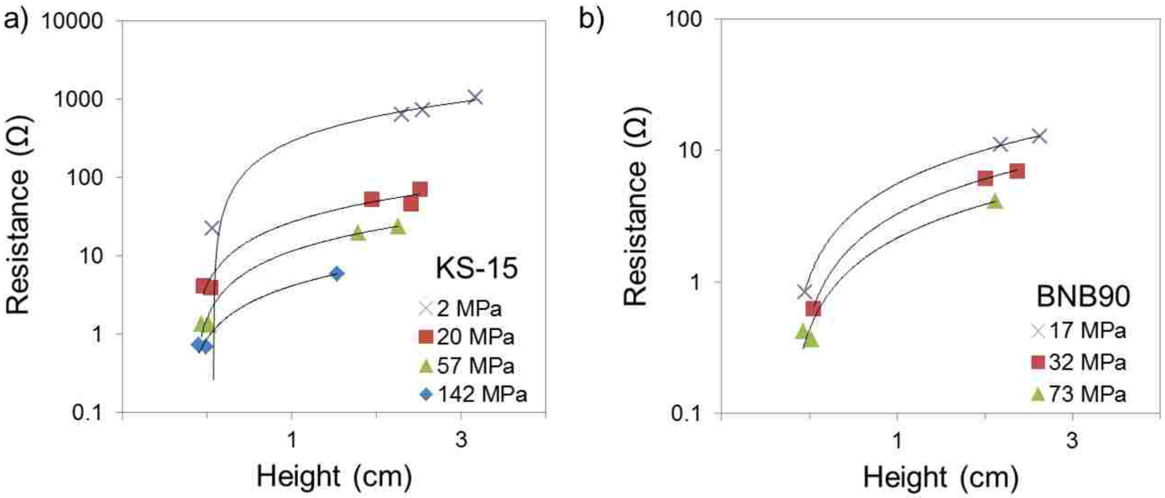

Figure 3.3: Resistance vs. cathode height for (a) KS-15 and (b) BNB90, using both thick and thin cathode samples. A log scale is used for resistance; the lines are linear least-squares fits to the data points.

Table 3.2 summarizes the results of the linear least-squares fits shown in Figure 3.3. In Table 3.2 the slope corresponds to $(\sigma_{\text{eff}} A)^{-1}$ while the y-intercept corresponds to R_c (based on Equation 3.2). Table 3.2 shows that R_c depends on pressure and carbon type or its conductivity. In an attempt to normalize R_c relative to these two effects and thus calculate an overall contact resistance for the apparatus, the x-intercept, h_c, was calculated for each of the correlations in Table 3.2.

Figure 3.4 is a plot of h_c vs. pressure for the two materials given in Table 3.2. The error bars are the standard deviations on h_c, which were calculated using the uncertainty in the resistance based on York's method [59]. It shows that h_c is fairly insensitive to pressure and carbon type. Furthermore using conservative estimates for extreme values of h_c, namely 0.3 and 0.1 cm, yields calculated σ_{eff} values that vary by 12% or less between the two extremes. Thus, it seems reasonable to treat h_c as a constant value for the purpose of interpreting our conductivity experiments. Because of the interest in high conductivity carbon additives, a h_c value closer to those of BNB90 was selected, specifically 0.25 cm. Note that this value accounts for contacts both above and below the sample. The value is physically reasonable when considering the idea of spreading length because it is larger than the EMD particle size (approx. $50\mu m$) and is smaller than the cathode sample diameter (approx. 0.635 cm). Comparing this height to that of the typical thick cathode heights (2 cm), those used in the electronic conductivity measurements, shows that the combined spreading length is about 10% of the total cathode sample height.

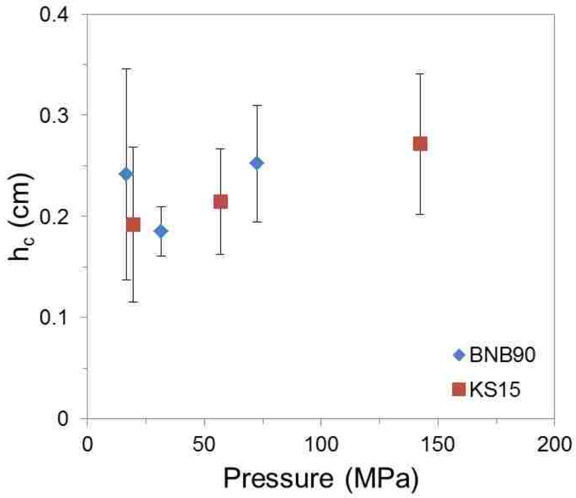

Figure 3.4: h_c or x-intercept from contact resistance experiments vs. pressure for BNB90 and KS-15. The error bars are the standard deviation from the least-square fits shown in Figure 3.3.

Radial cathode expansion. As the sample is compressed, some of the axial force contributes to the radial expansion of the cathode sample and thus the nylon sleeve. In order to accurately calculate porosity, one must know the volume of the sample, which in turn requires knowing the cross-sectional area. To correct the porosity calculations for this effect, the magnitude of the radial expansion was determined both experimentally and theoretically. Experimentally, after a cathode sample was compressed to a low porosity (approx. 20% overall porosity), the cathode-containing nylon sleeve was removed from the steel tube. Then, the nylon sleeve was measured using a micrometer. The nylon-sleeve radius had expanded by approximately 0.05 mm. To theoretically calculate the expansion of the cathode, the vertical and radial stresses were related, using relationships used in the field of soil mechanics as shown in the following equations:

$$\epsilon_{\mathrm{r}} = \frac{\sigma_{\mathrm{r}}}{E} = \frac{K_o \sigma_{\mathrm{z}}}{E} = \frac{\Delta r}{l_o}\,, \tag{3.3}$$

where ϵ_{r} and σ_{r} are the radial strain and stress of the nylon, respectively; K_{o} is the coefficient of earth pressure at rest; E is the Young's modulus for nylon (approx. 3 GPa); σ_{z} is the vertical stress (approx. 100 MPa); $\Delta r = r - r_o$ is the change in the cathode radius; r_o is un-expanded radius of the cathode or inside radius of the nylon sleeve; and l_o is the un-expanded thickness of the nylon (approx. 3.226 mm). In Equation 3.3, the first relationship is the standard stress-strain relationship in the radial direction. The second equality relates the vertical stress to the radial stress, using the coefficient of earth pressure at rest. $K_o = 0.5$ for typical soil-like materials, which we assume to be accurate for EMD-based cathodes [60]. The third relationship in Equation 3.3 is the definition of strain in the radial direction. Since the expansion of the cathode depends on the compression pressure, the cathode porosity at each stage of the compression experiment was calculated using a rearrangement of the above equation:

$$\Delta r = \frac{l_o K_o}{E}\,\sigma_z\,. \tag{3.4}$$

In above experiment, $\sigma_z = 209\,MPa$. The corresponding theoretical expansion, Δr, was calculated to be 0.056 mm, which is similar to the experimental expansion value (0.05 mm), showing that Equation 3.4 is a reasonable approach to the problem. For analyzing all other compression experiments in this work, $l_o K_o/E = 5.38 \cdot 10^{-4}\,\text{mm/MPa}$ was used in Equation 3.4 to relate cross-sectional sample area to applied axial stress. This correction to the area modestly increases the calculated porosity, particularly at high-pressure low-porosity conditions.

Data analysis. The analysis of the raw position, force, and voltage data was performed, using Microsoft Excel and VBA. Based on the change in slope between sequential points, points corresponding to the relaxed and first-compressed regions for each completed sequence of steps (1-5) were identified. Specifically, a compressed region corresponds to a region that was preceded by a negative slope while a relaxed region corresponds to a region preceded by a positive slope. Then, the points at the lowest force, or mechanically equilibrated points, were selected from the relaxed and compressed regions. For the compressed regions, the points from the initial compressing step (step 2) rather than re-compressing (step 5) are used to avoid any re-compressing effects. The results of this analysis are displayed in Figure 3.5, which shows the selected position points and the corresponding force and voltage data points. Based on Figures 3.5c and 3.5d illustrate that the difference in resistance between the compressed and relaxed conditions increases with decreasing porosity. This suggests, as expected, that lower porosity samples are better electronically connected, so additional pressure amplifies these connections and thus the conductivity performance.

After the data had been separated as compressed or relaxed, all the experimental runs for a given carbon type were analyzed as follows. Typically, two to four runs were performed for each carbon additive to ensure repeatable results. The porosity, specifically the inter-particle porosity, was calculated from the height, using Equation 3.5. The inter-particle porosity is defined in Equation 3.5:

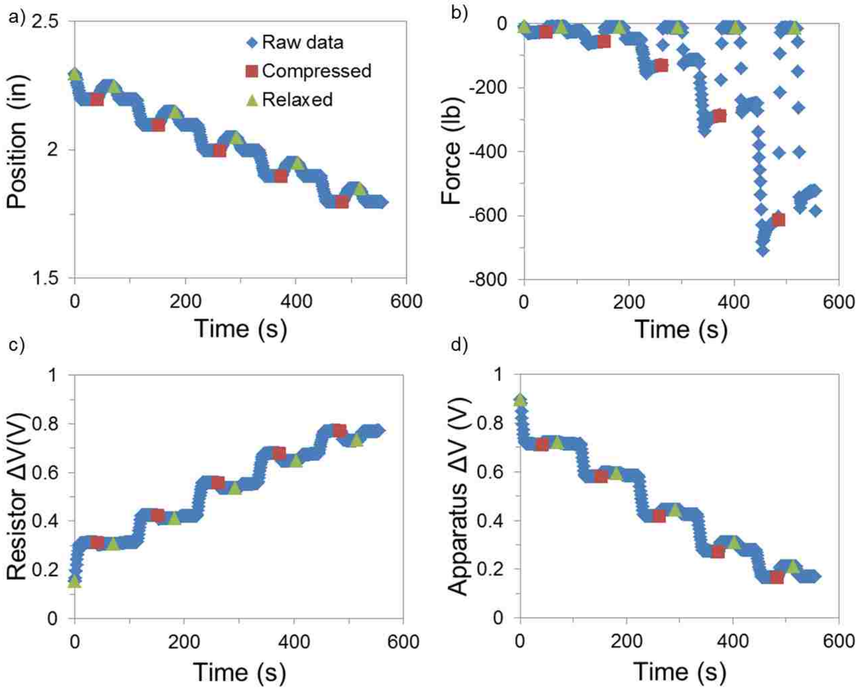

Figure 3.5: Validation of the data analysis used to select the compressed and relaxed data points, specifically the points for (a) position and the corresponding (b) force, (c) the voltage over the resistor and (d) the voltage over the apparatus.

$$\epsilon_{\text{inter}} = 1 - \frac{m}{\rho_{\text{p}} \pi r^2 h}\,, \tag{3.5}$$

where ϵ_{inter} and ρ_{p} is the inter-particle porosity and weighted-particle density, respectively. The motivation for using inter-particle porosity rather than overall porosity is briefly discussed with Figure 3.6, and in detail in Section 3.4.

The electronic conductivity was calculated using the following equation:

$$\sigma_{\text{eff}} = \frac{h + h_c}{R_{\text{app}} A}\,. \tag{3.6}$$

This equation corrects the conductivity using the previously determined contact resistance, h_{c}. R_{app} was calculated using the following equation:

$$R_{\mathrm{app}} = \frac{V_{\mathrm{app}}}{V_{\mathrm{R}}} R_{\mathrm{R}} \,, \tag{3.7}$$

where V_{app} and V_{R} are the measured voltage over the apparatus and over the resistor, respectively, and R_{R} is the external resistor resistance (10.3 Ω). A 10.3-Ω resistor was selected because the most design-relevant electronic conductivity values are those at a low overall porosity (approx. 20%). At this low porosity, the resistances of the various cathodes were approximately 1 to 10 Ω. Matching the external resistance to the sample resistance maximizes sensitivity in measured R_{app} values. In addition, to avoid resistor heating effects at high currents, a high-power resistor (10 W) was used as well as a low (approx. 1 V) supplied voltage (see Figure 3.1b).

Figure 3.6 shows the electronic conductivity for the various carbon additives listed in Table 3.1. Two to four runs were performed for each carbon additives to ensure accurate results. The data points at similar porosities from the various runs were averaged (arithmetic mean) for each carbon type to generate the data points shown in Figure 3.6. In addition, the porosities of the relaxed samples were assumed in each case to be nearly the same as the porosity of the compressed sample immediately before that relaxation step. This adjustment assumes that the porosity does not change during the relaxation step, or more specifically that the samples does not significantly expand when the pressure is reduced. This is likely reasonable given the slow rate (one-tenth of the total distance per second) at which the sample was compressed and relaxed.

Figure 3.6 illustrates the inverse relationship of electronic conductivity and porosity. Specifically at higher porosities, more pores are present and they impair the electronic pathways while at lower porosities few pores are present, providing better connected electronically conductive pathways. Generally, the various carbon additives appear to converge toward a similar maximum conductivity, except for graphene nanopowder and BNB90. Notably, both these exceptional carbon additives can be considered expanded graphites. Overall, the relative similarity of conductivities at compressed and relaxed conditions, especially at high porosities which correspond to higher contact resistance or lower pressure, suggests that the uncertainty in the contact resistance is not a significant bias.

The use of inter-particle porosity rather than overall porosity in Figure 3.6 and later Equation 3.8 is explained in detail in Section 3.4. In summary, inter-particle porosity does not include porosity within EMD particles, which is part of the overall porosity. Intra-particle porosity is relatively fixed and is not expected to effect changes in electronic pathways as does inter-particle porosity upon compression of the sample. The inter-particle porosity can be readily determined from SEM/FIB images, or can be estimated from knowledge of particle density and bulk density. The apparent inter-particle porosity can become negative at high amounts of compression if intra-particle pores partially or completely collapse, thus decreasing the apparent "solid" or non-inter-particle pores volume. Further comparison of the various carbon additives conductivities to their microstructural and material properties is provided in Section 3.4.

Finally, the experimental electronic conductivity values in Figure 3.1 were fit with the following Bruggeman-type relation or power-law:

$$\sigma = \sigma_o(1 - \epsilon_{\mathrm{inter}})^b \,, \tag{3.8}$$

where σ_o and b are parameters and $\epsilon_{\mathrm{inter}}$ is inter-particle porosity. The electronic conductivity data was fit using non-linear least-squares regression analysis. The quality of the fit was determined using coefficients of determination (R^2). The R^2 for the various carbon additives in Table 3.1 ranged from 0.93 to 0.998 for compressed values and from 0.84 to 0.988 for the relaxed values, indicating an extremely accurate fit. The mean R^2 value for all the fits (both compressed and relaxed) is 0.96, and the minimum R^2 value is 0.84. Table 3.3 provides parameters for each carbon type reported in Table 3.1 at both compressed and relaxed conditions.

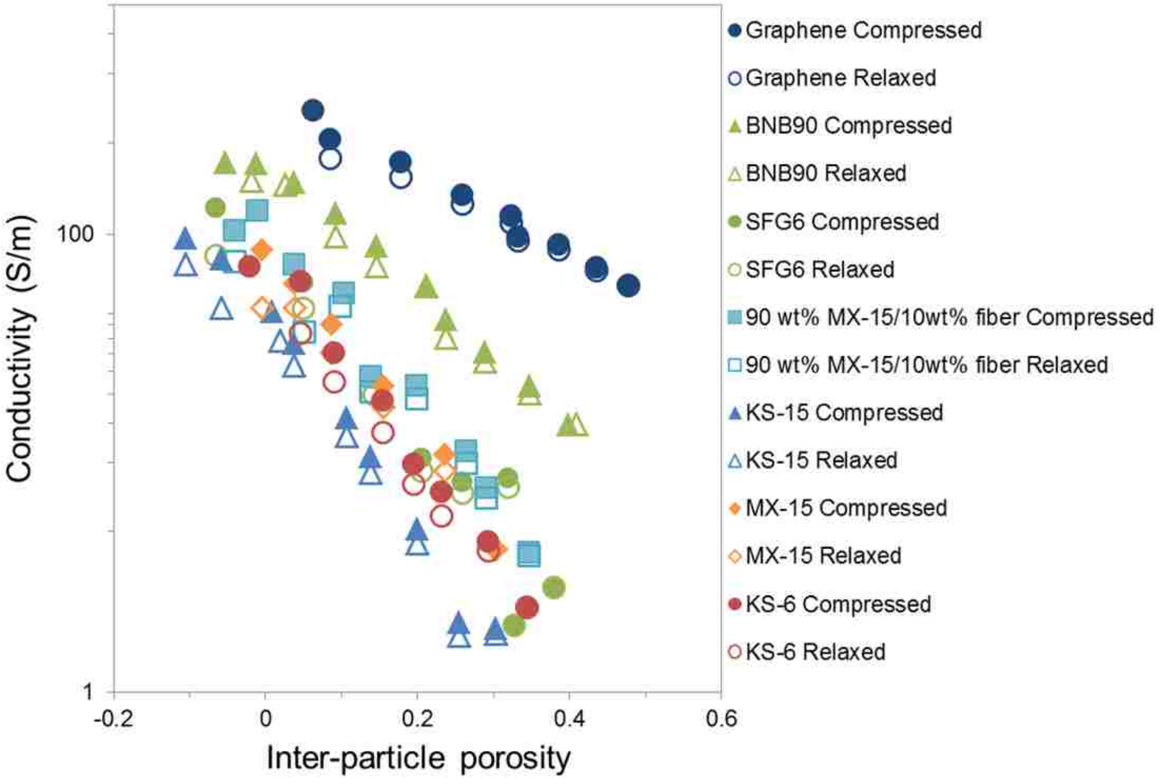

Figure 3.6: Electronic conductivity vs. inter-particle porosity at both compressed and relaxed conditions for the carbon additives listed in Table 3.1.

Physically, σ_o corresponds to the electronic conductivity at zero inter-particle porosity. At this condition, the EMD and carbon particles are closely packed and well connected. Thus, σ_o describes essentially a maximum practical electronic conductivity. As such, it is used as a suitable performance metric to compare the performance of the various carbon additives investigated. These comparisons are discussed in detail in Section 3.4.

Statistical significance. To determine if the different performance of the various carbon additives was statistically significant, a joint confidence region was created for each fit (both compressed and relaxed) [61]. A joint confidence region represents the correlated confidence intervals of both parameters: σ_o and b. In this case, a 95% confidence level was used. (Note: traditional plus/minus-errors neglect the correlation or interdependence of the two parameters.) As with standard deviations and other errors, overlapping confidence regions indicate

Table 3.3: Bruggeman-fitting parameters for each carbon additives investigated at compressed and relaxed conditions (sort from largest to smallest σ_o).

Carbon Additive	σ_o(S/m)	b
Graphene Compressed	380.88	3.06
Graphene Relaxed	274.45	2.37
BNB90 Compressed	184.98	4.80
BNB90 Relaxed	165.19	5.00
90/10 wt% MX-15/fiber Compressed	91.09	5.97
SFG6 Compressed	82.19	7.37
MX-15 Compressed	82.15	7.83
KS-6 Compressed	66.79	7.52
90/10 wt% MX-15/fiber Relaxed	60.95	5.25
SFG6 Relaxed	56.62	6.09
KS-6 Relaxed	52.35	8.25
MX-15 Relaxed	51.18	6.08
KS-15 Compressed	44.64	8.18
KS-15 Relaxed	33.33	7.90
EMD Compressed	0.38	5.93
EMD Relaxed	0.12	3.98

a lack of statistical significance while independent or non-overlapping regions indicate that the two correlations are statistically different. As shown in Figure 3.7a, the compressed and relaxed parameters were significantly different from each other for each carbon additive, except for TIMCAL BNB90. This suggests that compression, or more generally pressure, significantly affects electronic conductivity. This agrees with the physical insight that electronic conductivity increase with the number of particle-to-particle contacts, which would increase with increasing pressure.

Looking only at the compressed-cathode correlations, the pairs that were not significantly different were the TIMCAL MX-15/Pyrograf fiber mix and TIMCAL MX-15, TIMCAL MX-15/Pyrograf fiber mix and TIMCAL SFG6, TIMCAL SFG6 and TIMCAL MX-15, as well as TIMCAL SFG6 and TIMCAL KS-6 (see Figure 3.7b). Likewise, these pairs were not statistically different at relaxed conditions, neither were TIMCAL MX-15 and TIMCAL KS-6 (see Figure 3.7c). SFG6 and MX-15 have similar particle morphologies and Scott densities, suggesting these physical properties may have a predictable effect on electronic conductivity. Overall, this analysis suggests that the various carbon additives investigated, which have a range of physical properties (see Table 3.1), produce statistically different electronic conductivities. Thus, a statistically significant improvement may be achieved by optimizing the carbon additive material and its corresponding microstructural properties.

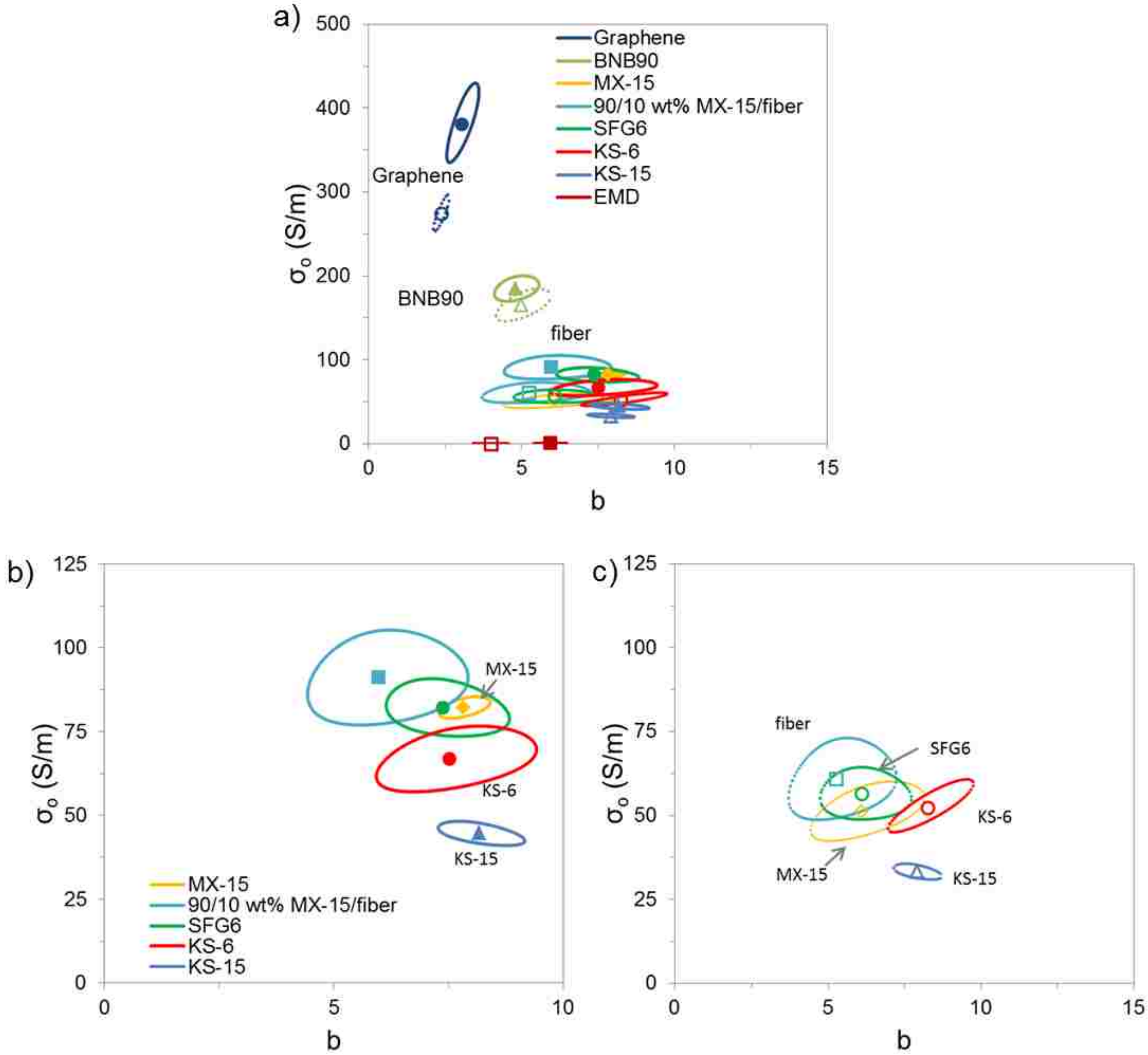

Figure 3.7: (a) 95% joint confidence regions on Bruggeman-fitting parameters, σ_o and b, are shown to determine if the various carbon additives are statistically significant. Also, zoomed-in 95% joint confidence regions on fitting parameters, σ_o and b, are shown for the (b) compressed and (c) relaxed correlation conditions. Solid lines and filled symbols indicate compressed values while broken lines and open symbols indicate relaxed values.

3.3.2 Ionic transport or conductivity

As discussed in Chapter 2, both electronic and ionic transport influence battery performance. Furthermore, viable improvements in electronic conductivity must not impair the necessary ionic conductivity. To quantify the ionic conductivity, an apparatus was developed based on a method previously developed by our research group [17, 62]. (These references provided a more detailed description of the method.)

In summary, this method places a cathode sample sandwiched between separators, which are sandwiched between two electrodes in this case Ag/AgCl. Figure 3.8 shows a schematic of the apparatus used. Separators are placed with the glossy side toward the cathode. The electrodes, cathode, and separators are then placed inside a plastic sleeve, and 1 M KCl is added until the entire apparatus is moist. A 220-g weight is then placed on top of the apparatus to ensure constant force is being applied throughout the experiment. The ionic conductivity experiment involves a polarization step and an interrupt step. The polarization step involves pushing ions, in this case KCl, through the cathode, and the interrupt or relaxation step allows them to diffusion back through the cathode. Polarization is accomplished by passing DC current through the system at 5 mA for 15 minutes. Then, the system is allowed 20 minutes to relax before the current is run in the opposite direction for 15 minutes. Again, the system is given 20 minutes to relax.

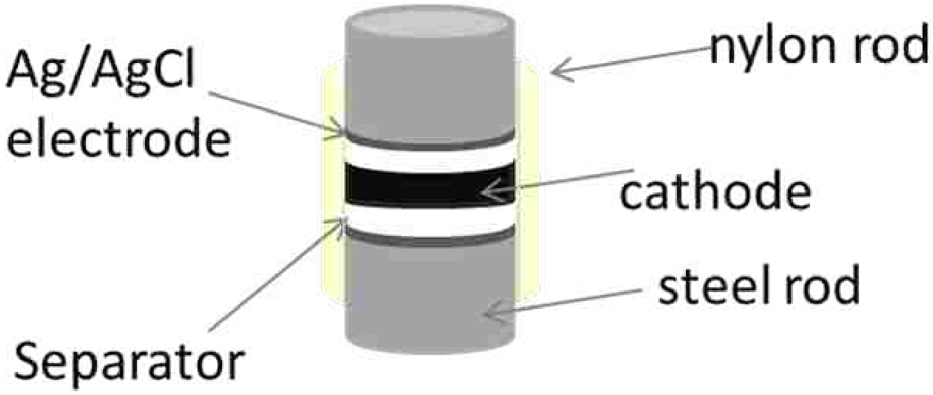

Figure 3.8: Schematic of the ionic conductivity apparatus.

A model was adapted from the previously developed method to interpret this polarization-relaxation process, and calculate a tortuosity, which is an effective geometric parameter [17]. Tortuosity is defined as:

$$\kappa^{\mathrm{eff}} = \frac{\kappa\epsilon}{\tau}\,, \tag{3.9}$$

$$D^{\mathrm{eff}} = \frac{D\epsilon}{\tau}\,, \tag{3.10}$$

where κ^{eff} and D^{eff} are the effective conductivity and diffusivity, κ and D are the intrinsic conductivity and diffusivity (of the electrolyte), ϵ is the porosity, and τ is tortuosity. Tortuosity is a generalized, or effective, geometric property for the system, and describes the fact that pores are not straight nor of uniform cross section. Tortuosity enables ionic conductivity to be calculated for various porosities and intrinsic ionic conductivity for a given ion (see Equation 3.9).

Figure 3.9a shows the full relaxation curve for an ionic conductivity experiment for a proprietary cathode sample with an overall porosity of 27.5%. This plot shows the experimental value relative to tortuosity contours from the model. To correct for instrumental offset error, 0.5 mV was subtracted from the relaxation voltage. This correction allows the voltage to relax to zero. Currently, the model does not have the necessary data to accurately represent the charge or polarization steps nor the first few seconds of the relaxation steps, which are non-linear as apparent from Figure 3.9a. Nevertheless, it does have the necessary data to model the relaxation step that is essential to determine the ionic conductivities. The linear region of this voltage relaxation curve is shown in Figure 3.9b relative to the tortuosity contours calculated from the model. Tortuosity depends more the slope of the line rather than its exact vertical position (intercept). Figure 3.9b shows that the tortuosity of this sample is approximately 3±1. Using Equation 3.9 with τ equals 3 and ϵ equals 0.275, the effective ionic conductivity of the sample would be 5.75 S/m, using the intrinsic conductivity of 7 M KOH at 25°C (62 S/m), which corresponds to the electrolyte conditions in actual alkaline batteries [63]. Comparing the magnitude of the electronic and ionic conductivities can indicate which transport process is limiting or under-designed. Since the electronic conductivity is more than 50 times greater (300 S/m to 5.7 S/m) than the ionic conductivity, it suggests that this proprietary cathode is disproportionately designed to promote electronic conductivity compared to ionic conductivity.

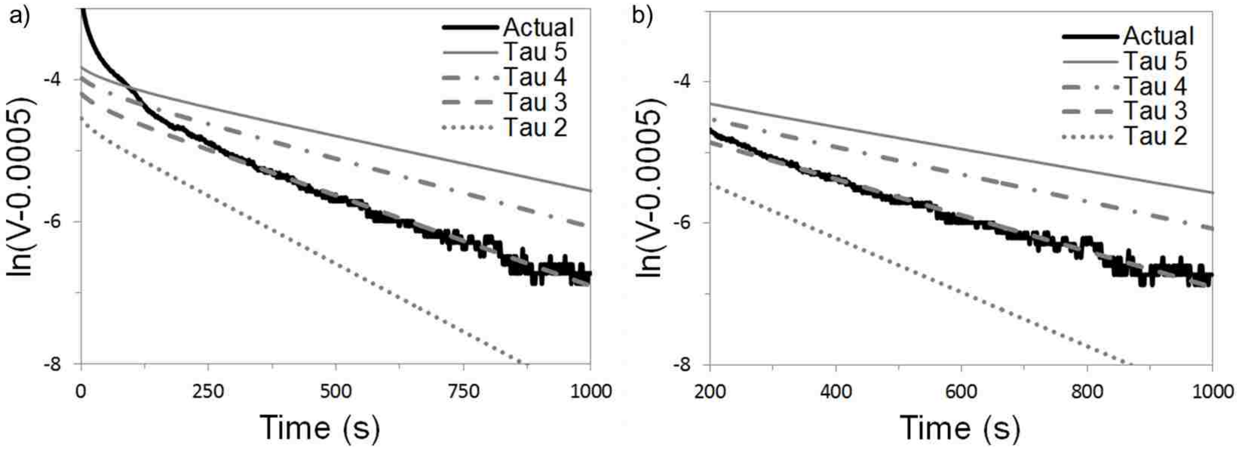

Figure 3.9: Schematic of the ionic conductivity relaxation step, (a) full curve and (b) linear region, compared to predict tortuosity contours.

3.4 Microstructure analysis

The electronic conductivity data from Section 3.3 provide a fundamental performance metric for evaluating the effect of various carbon additives and their microstructures. Specifically, the fitting parameter σ_o, which is essentially a maximum electronic conductivity, was used as a metric to compare the efficacy of the various carbon additives. This metric was used to assess the performance effects of both additive intrinsic material properties as well as the overall microstructure. It is helpful to be able to compare σ_o to observed microstructures in order to understand and explain observed differences between the different carbon additives.

The material properties used for comparison are those reported in Table 3.1. SEM/FIB microstructure analysis was used to visualize and understand the overall microstructure characteristics–including porosity, dispersion, and connectivity–of the carbon throughout the electrode. SEM/FIB stands for scanning electron microscopy/focused ion beam. SEM uses the interactions of an electron beam with a sample to produce an image. FIB involves using an ion beam to mill a sample in order to obtain a SEM image of the interior of the sample. Overall, SEM/FIB enables the imaging of sequential cross-sectional slices of a sample. This technique was used to analyze the microstructure of cathode samples. The SEM/FIB images shown here were generated by Yuan Wen, another student in our research group. These images were produced from samples compressed using a bench-top press rather than the MTS instrument, which was used for the electronic conductivity measurements. The microstructural characterization was primarily qualitative as more detailed quantitative analysis was beyond the scope of this work.

3.4.1 EMD nanoporosity

The most basic microstructural parameter is volume fraction. The fractions of total volume occupied by solids and pores can be calculated from macroscopic measurements of mass and volume (see Equation 3.1). SEM/FIB images enable a more localized, detailed analysis. As shown in Figure 3.10, SEM/FIB images fail to show all of the apparent porosity without significant magnification, suggesting that EMD particles contain significant porosity that is not always observed in typical SEM/FIB images. Furthermore, it is difficult to quantify the amount of EMD intra-particle porosity from SEM/FIB. To better understand this, a series of experiments were performed.

SEM/FIB and electronic conductivity measurements, at various porosities, were performed on the pure EMD pellet to determine the affect of EMD nanoporosity. SEM/FIB images of compressed EMD show inter-particle and intra-particle pores (see Figure 3.10). In fact, there appears to be a distribution of both inter- and intra-particle pore sizes. Figure 3.10c clearly shows nanoporosity within the EMD. The nanoporosity of EMD was confirmed using a simple water absorption test and also by the literature [64].

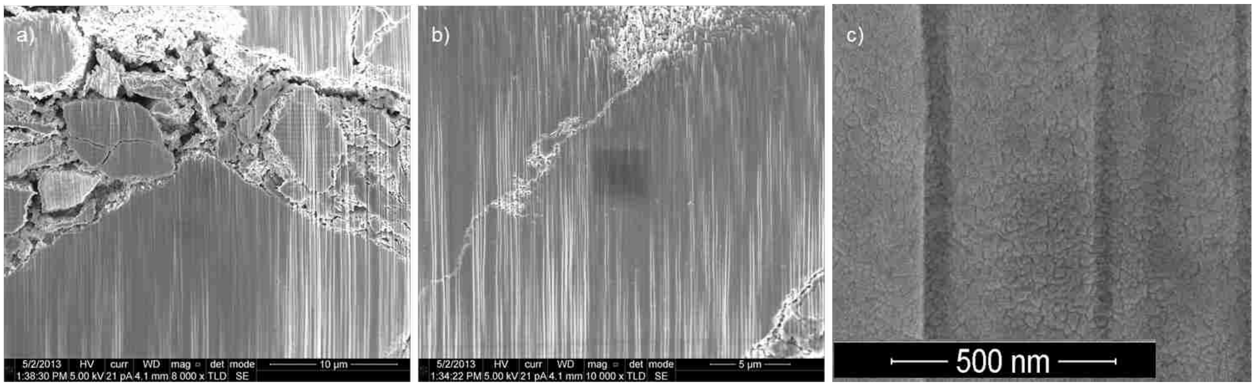

Figure 3.10: SEM/FIB for Tronox EMD: (a) shows the large inter-particle and intra-particle pores, (b) shows a close-up of the intra-particle pores, and (c) shows the internal nanopores within EMD (appearing as cracks).

Table 3.4: Various density definitions [64, 65]

Density	Defined volume	Value ($g\,cm^{-3}$)	Ref.
Crystalline	crystallite only	4.9	[64]
Skeletal (or real)	crystallites and closed pores	4.5	[64]
Particle	crystallites plus intra-particle pores	3.3	[64]
Tapped	bulk volume of tapped or pressed powder	2.4	[64]
Scott	“as-poured” volume	1.62	[65]

The water absorption test entailed compressing one of the carbon-based cathodes with a bench-top press to a low overall porosity (24.5%), and then wetting it with water until additional water ceased to be absorbed into the sample. The volume of water added corresponds to an overall porosity of approximately 24.8%, which is fairly similar to the calculated overall porosity of 24.5%, suggesting again the presence of intra-particle porosity.

To more precisely analyze the intra-particle porosity, electronic conductivity measurements were performed on EMD over a range of porosities and thus apparent densities. Figure 3.12 shows the resulting electronic conductivity vs. apparent EMD density plot. The apparent density used in this plot was determined from the measured heights and areas of the EMD samples. The various density regions displayed in Figure 3.12 are defined in Table 3.4, and illustrated in Figure 3.11.

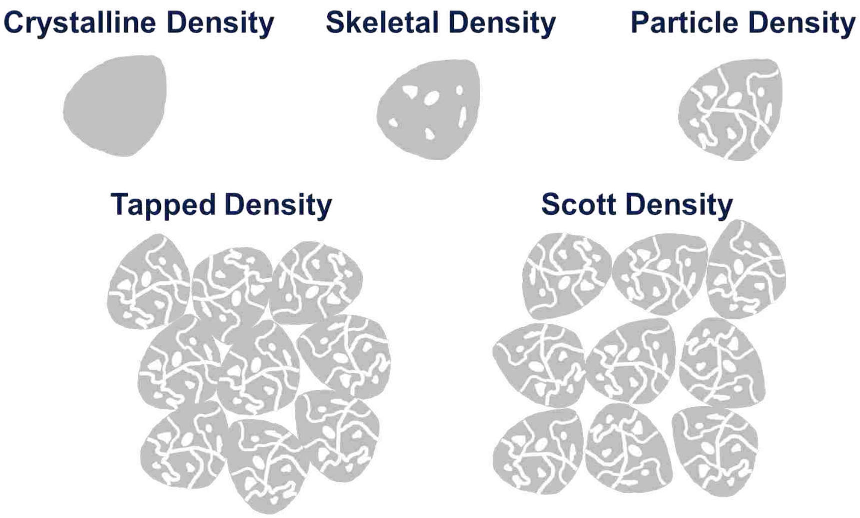

Figure 3.11: Schematic of various types of porosity or density corresponding to the definitions in Table 3.4.

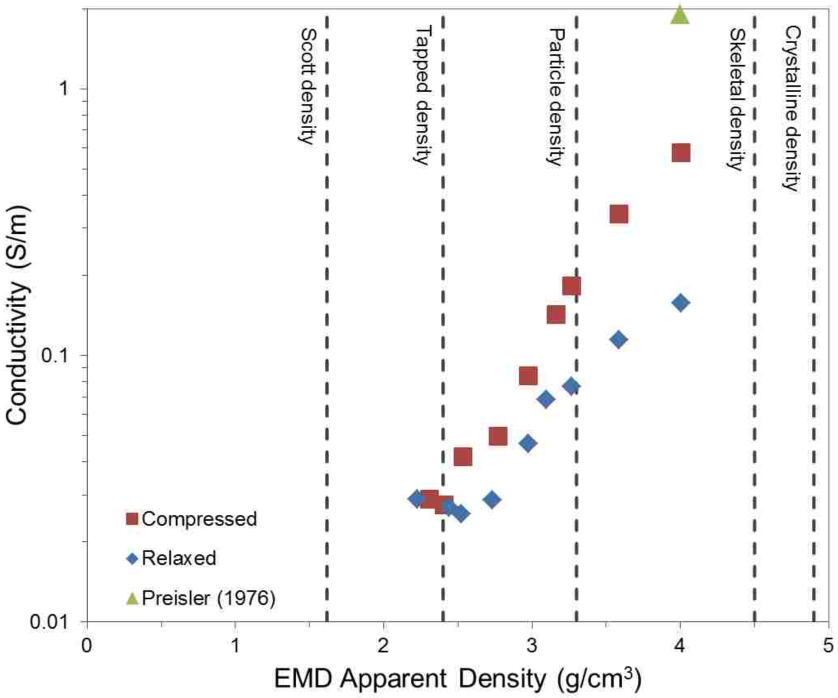

Figure 3.12: EMD conductivity vs. apparent density. The experimental densities below the particle density indicate intra-particle porosity within the EMD. Preisler (1976) is Ref. [66].

Figure 3.12 suggests the collapse of intra-particle pores at a low overall porosity, since apparent density exceeds the particle density. For both the compressed and relaxed data points, the highest-density points have an apparent inter-particle porosity of -12% while the lowest-density points have an inter-particle porosity of approximately 36%, which is near the tapped density. The negative inter-particle porosity indicates a collapse of internal pores, since the effective EMD bulk density is higher than particle density, and thus closer to the skeletal density.

Since the intra-particle porosity is relatively fixed and is not expected to effect changes in electronic pathways as does inter-particle porosity upon compression of the sample, the inter-particle porosity proved to be a better metric to compare the conductivity performance to cathode microstructure. In addition, it is difficult to quantify the intra-particle porosity from a SEM/FIB image due to low contrast within the EMD. Based on Figure 3.12, a revised value of EMD particle density, 3.7 $\mathrm{g\,cm^{-3}}$, rather than the value of 3.3 $\mathrm{g\,cm^{-3}}$ given in Table 3.4 was used to calculate the inter-particle porosities reported in Figure 3.6. The overall and inter-particle porosities are related by Equation 3.11

$$\frac{1-\epsilon_{\mathrm{tot}}}{1-\epsilon_{\mathrm{inter}}} = \frac{\rho_{\mathrm{s}}}{\rho_{\mathrm{p}}} \,. \tag{3.11}$$

In summary, the presence of internal pores within the EMD particles is a significant material and microstructural property that directly affects the conductivity and performance of alkaline battery cathodes. For instance for a BNB90-based cathode, the inter-particle porosity is 12.5% while the overall porosity is 27.1%; hence, intra-particle porosity accounts for 14.6% of the cathode. Thus, the internal nanoporosity nearly doubles the volume of pores compares to the inter-particle porosity, yielding a larger overall porosity.

3.4.2 Effect of carbon-additive material properties and cathode microstructures

Large flake graphite. TIMCAL BNB90 is an expanded flake graphite with a large (approx. 90-μm) particle diameter. It gives the second highest electronic conductivity (σ_o): 184.98 and 165.19 S/m for the compressed and relaxed conditions, respectively. Figure 3.13 shows the overall microstructure of EMD/BNB90-cathode. The microstructure shows relatively long carbon "highways" that likely produce the high electronic conductivity of this carbon additive. The overall porosity of this sample is 27.1%, and an inter-particle porosity of 12.5%. The overall porosity seems high based on the visible pores in Figure 3.13a, suggesting again the presence of internal nano-porosity within the EMD.

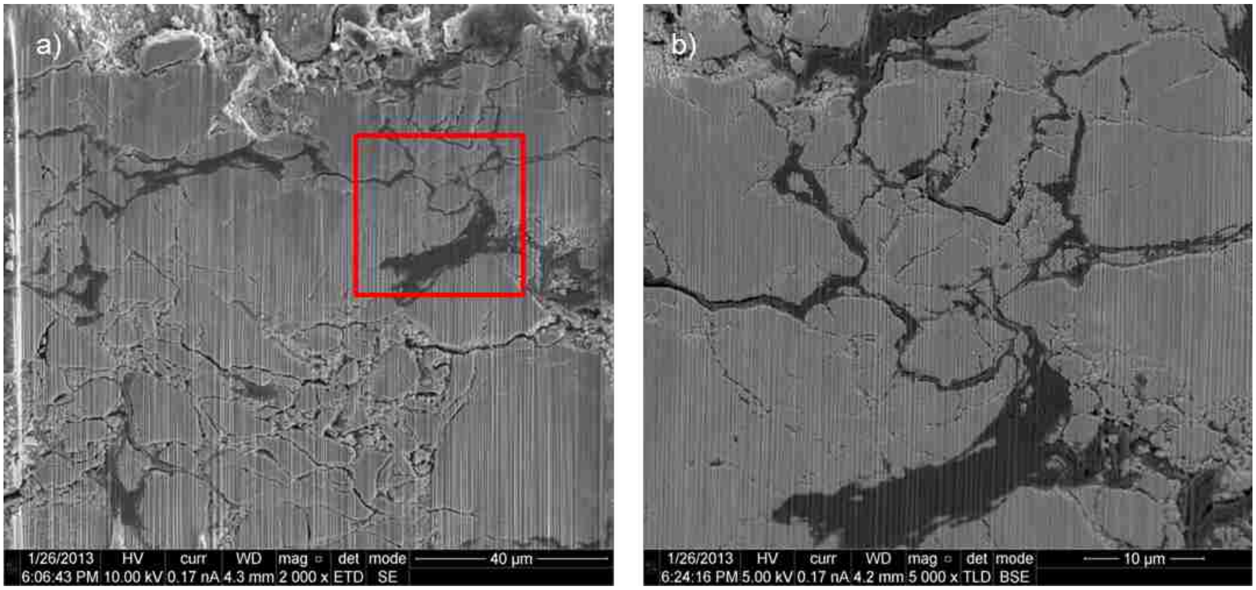

Figure 3.13: SEM/FIB for TIMCAL BNB90 shows the (a) bulk microstructure and (b) a close-up of the pore and carbon domains. (For reference: the gray is EMD, the black is carbon, and the pores appear a dark gray.). This cathode had an overall porosity of 27.1%, and an inter-particle porosity of 12.5%.

Particle diameter and morphology. The comparison of four different TIMCAL graphites enables the elucidation of the effect of particle diameter and morphology (or aspect ratio) on electronic conductivity. Specifically, TIMCAL MX-15 and SFG-6 have similar anisometric flake morphologies, but different particle sizes (17 and 6.5 μm, respectively) while TIMCAL

Table 3.5: The effect of carbon-additive particle size and morphology on electronic conductivity.

Carbon Additive	$d_{90}(\mu m)$	Shape	σ_o(S/m)	
			Compressed	Relaxed
TIMCAL SFG-6	6.5	flake	82.19	56.62
TIMCAL MX-15	17	flake	82.15	51.18
TIMCAL KS-6	6.5	spheroid	66.79	52.35
TIMCAL KS-15	17	spheroid	44.64	33.33

KS-15 and KS-6 have irregular spheroid morphologies with the same respective particle sizes just mentioned. Table 3.5 compares the σ_o for each of these carbon additives. This comparison indicates that smaller diameter particles and flake or higher-aspect-ratio graphites produce higher electronic conductivity. Yet, the change in conductivity was more pronounced for the spheroid rather than for flake graphites. Specifically, decreasing the particle size increases the conductivity (σ_o) by 50% for spheroid additives, but only by 0.04% for the flakes additives (compressed conditions). For the relaxed conditions, decreasing the particle size increases the conductivity by 57% and 11%, respectively. This illustrates the substantial improvement on conductivity achieved by decreasing the particle size. In addition, it illustrates the intrinsically better performance of flake graphites compared spheroid graphites. In fact for compressed conditions, the conductivity of the higher-aspect-ratio flake-based cathodes is approximately 23 to 84% greater (for the 6.5 and 17 -μm diameter particles, respectively) than the conductivity of the spheroid-based cathodes. At relaxed conditions, the respective values are 8% to 54% greater from flake compared to spheroid-based cathodes.

Nevertheless, Figure 3.6 and 3.14 show that the electronic conductivity is fairly similar for each of these four carbons additives. Additionally, BNB90 and graphene have widely different particle diameters despite having the two highest conductivities. Thus, particle diameter does not appear to be the most significant physical property in terms of electronic conductivity.

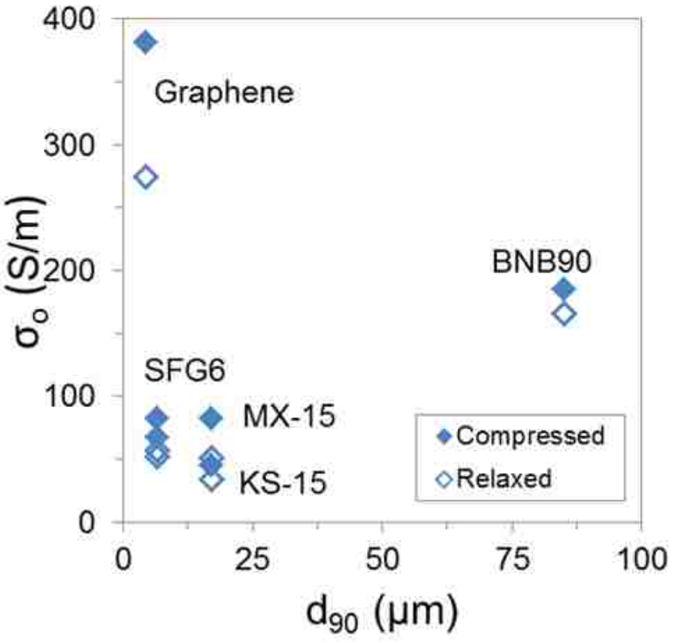

Figure 3.14: Electronic conductivity vs. particle diameter for various carbon additives except the fiber mixture, which did not have an exact particle diameter.

The SEM/FIB images were compared to relate the electronic conductivity performance to the cathode microstructures for these four carbon additives. Figure 3.15 shows the overall microstructure of the four carbon additives. The smaller carbon-additive particles appear to be more dispersed, providing enhanced long-range, electronically continuous pathways with good particle-to-particle contacting. Notably, the KS-6 graphite (smaller spheroids) appears more dispersed compared to the MX-15 graphite (larger flakes), yet the MX-15-based cathode has a higher conductivity (see Figure 3.15). This may be due to the larger aspect ratio of MX-15, creating more long-range electronic connectivity, which enhances electronic conductivity.

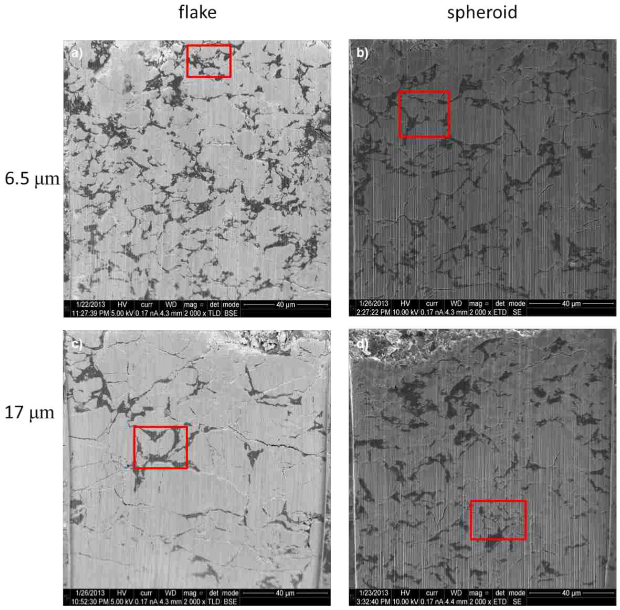

Figure 3.15: SEM/FIB images of (a) TIMCAL SFG6, (b) TIMCAL KS-6, (c) TIMCAL MX-15, and (d) KS-15, comparing the effect of carbon additive particle size and morphology on the cathode microstructure. The boxes indicate regions used to create the zoomed-in image in Figure 3.16. The respective inter-particle porosities are 11.8, 10.5, 11.8, and 12.4% while overall porosities are 26.5, 25.4, 26.5, and 27%. Hence on average the intra-particle porosity is approximately 15%. The conductivity decreases from left to right, and up to down.

Figure 3.16 shows zoomed-in SEM/FIB images of the four carbons, supplying a better view of the particle-to-particle contacts and inter-particle porosity. The spheroid particles appear to be more compact or aggregated compared to the longer or more elongated flakes. The elongated-nature of the flake graphite likely creates more surface area in contact with adjacent particles, facilitating electronic conductivity. Again, this is likely the reason for higher conductivity of TIMCAL MX-15 compared to KS-6 graphite-based cathodes.

Bulk carbon density and surface area. The effect of carbon bulk or Scott density and BET surface area were evaluated by comparing the physical properties reported in Table 3.1 to the maximum conductivity, σ_o. Figure 3.17a compares electronic conductivity to the bulk carbon additive density. In general, this comparison illustrates that electronic conductivity appears to generally increase with decreasing bulk carbon density. These bulk densities correspond to bulk volume fractions. While not strictly accurate, the following analysis illustrates the potential impact of lower density carbon additives. Assuming no inter-particle porosity (so the cathode volume is either EMD or carbon) and using the Scott densities for both EMD and several carbon additives, the respective cathode bulk volume fractions were calculated for this "as-poured" condition, which would likely be similar to the case observed during the mixing of EMD and carbon powders. Specifically for 95 wt% EMD cathodes, the following are the respective bulk volume fractions for graphene, BNB90, SFG6, and KS-15 based cathodes: 64, 71, 51, and 42 vol% (listed in order of decreasing conductivity). Generally, the conductivity increases with increasing bulk carbon volume fraction (or decreasing bulk density), which may be due to better mixing or contacting between the more volumetrically similar amounts of "as-poured" bulk carbon and EMD.

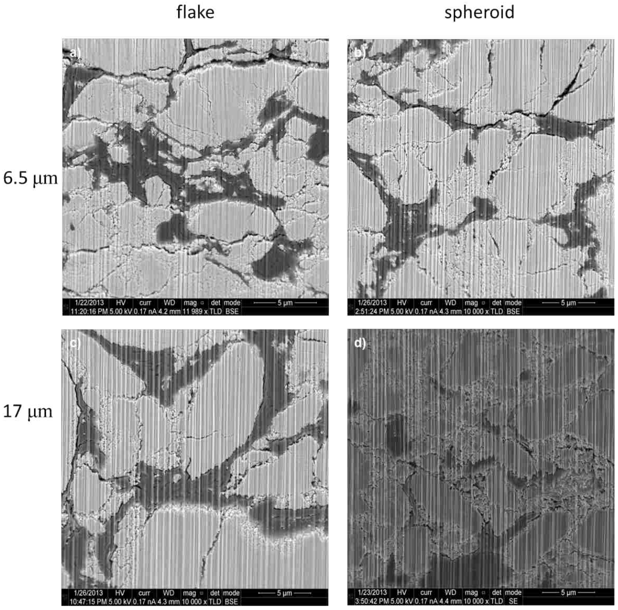

Figure 3.16: Zoomed-in SEM/FIB images of (a) TIMCAL SFG6, (b) TIMCAL KS-6, (c) TIMCAL MX-15, and (d) KS-15 enable the comparison of the effect of carbon-additive particle size and morphology on the cathode microstructure.

Figure 3.18 does not show a clear microstructural trend for the various carbon bulk volume fractions. In general, graphene and BNB90 have the highest bulk volume fractions and have more aggregated, yet elongated carbon domains compared to the SFG6 and KS-15 images, which show less aggregated and more dispersed carbon domains. This suggest that a more continuous, aggregated carbon domain provides better conductivity performance compared to extremely dispersed carbon additives. This reinforces the understanding that conductivity is controlled by both the distance between carbon particles (dispersion) along with the number of particle-to-particle contacts [7]. Again, the level of dispersion may be related to the bulk carbon density and volume fraction and possibly their effects on mixing. Furthermore, graphite is typically used as a lubricant and it may be that lower bulk densities provide more compressible volume that can be used to more effectively mold around the larger EMD particles as the sample is compressed, thus providing better particle-to-particle contacting.

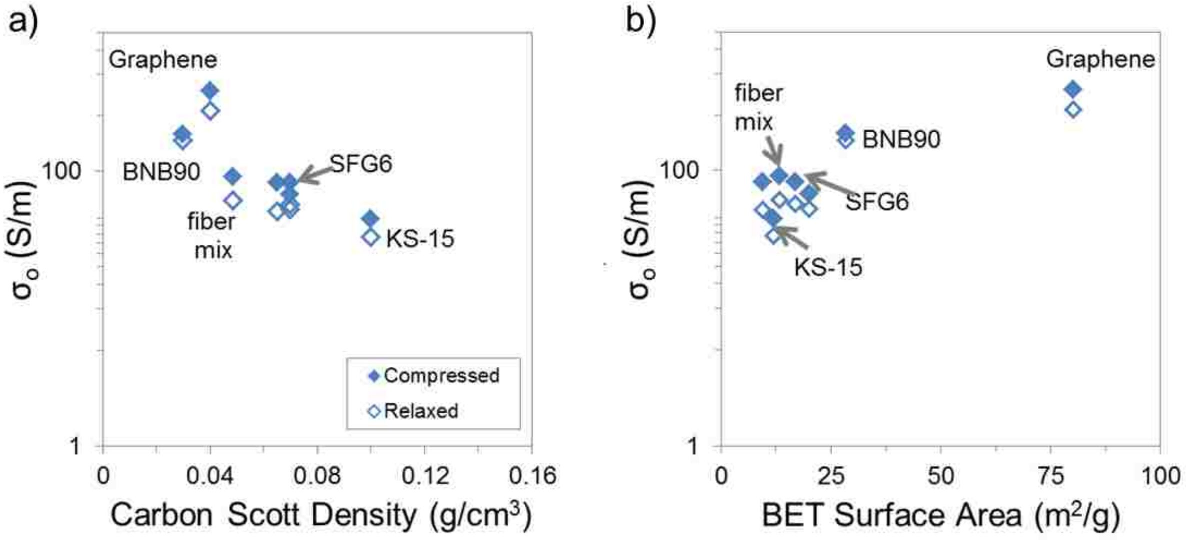

Figure 3.17: Electronic conductivity vs. (a) Scott density and (b) surface area for the various carbon additives investigated.

In terms of surface area, Figure 3.17b suggests that the dependency of electronic conductivity on surface area appears to have a threshold value. Below 25 $m^2\,g^{-1}$, there is no clear dependence of conductivity on surface area, yet above this value conductivity increases directly with surface area. The improved conductivity performance with higher-surface-area carbon additives may be due to the larger surface areas, facilitating better particle-to-particle contacts and thus more effective localized electronic pathways. For a graphene-based cathode at the compressed condition, this effect appears to be magnified.

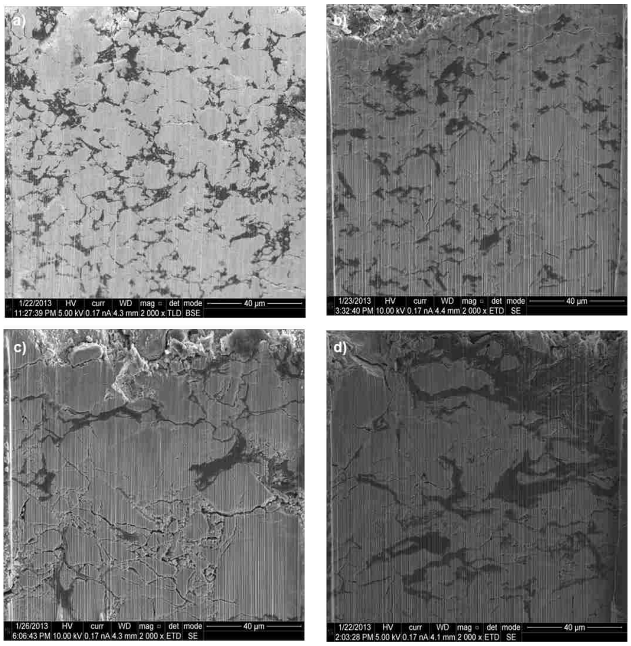

Figure 3.18: SEM/FIB images of (a) TIMCAL SFG6, (b) TIMCAL KS-15, (c) TIMCAL BNB90, and (d) Graphene Supermarket graphene nanopowder based cathodes.

Fiber mixture. A mixture of TIMCAL MX-15 and Pyrograf nanofiber (PR-19-XT-LHT) was used to evaluate any synergistic conductivity effects obtained by using nanofibers. Only 10 wt% of the total 5 wt% of carbon additive was fiber because when a 50/50 wt% carbon mixture was used the cathode did not hold together. The nanofibers were roughly 50-200 μm long and had a 150-nm diameter. The addition of the small fraction of fibers improved the electronic conductivity (σ_o) relative to the MX-15-based cathodes by 11% and 19% for the compressed and relaxed conditions, respectively. The improved performance of this mixture relative to pure MX-15 carbon additive is likely due to synergistic carbon pathways produced (i.e. long-ranged fiber connectivity and localized particle-to-particle MX-15 connectivity). Even greater improvements may be obtained by increasing the ratio of fiber to MX-15 from 1/9 to something less than 1/1, at which a structurally stable cathode is hard to make. Additionally, use of a smaller-particle-size carbon rather than MX-15 would likely improve performance. SEM/FIB images of the fiber-based cathode microstructure are shown in Figure 3.19. The fibers are difficult to see in the zoomed-out image, but the magnified image shows the network of fibers.

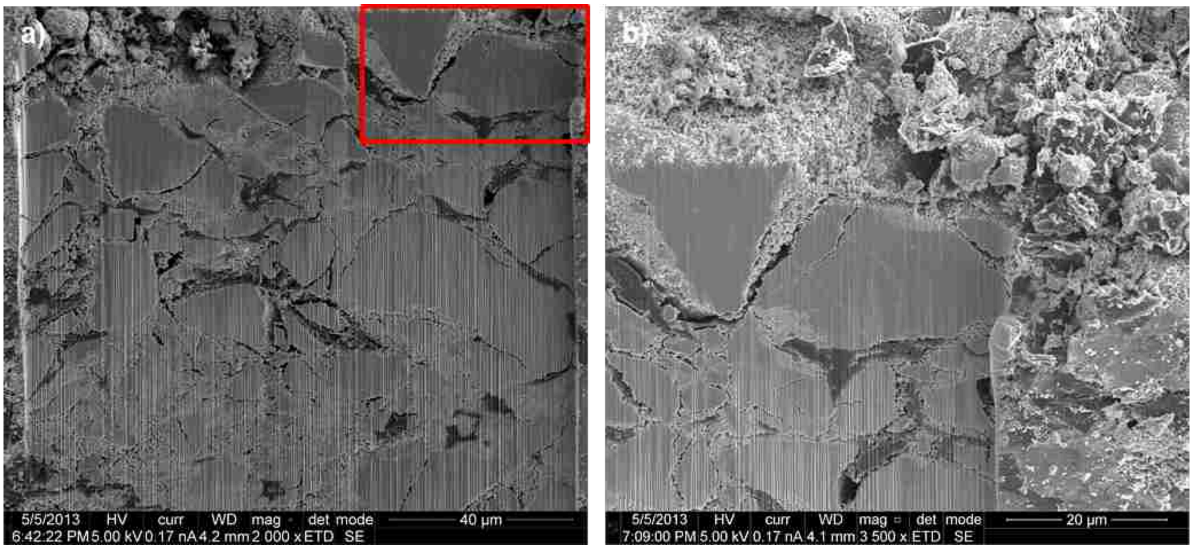

Figure 3.19: SEM/FIB of 10/90 wt% Pyrograf nanofiber/TIMCAL MX-15 base cathodes, showing the (a) overall microstructure and (b) magnified view of fibers. The inter-particle porosity is 16% while the overall porosity is 30%.

Graphene nanopowder. Graphene was investigated as a promising volumetrically efficient carbon additive due to its reported high electronic conductivity [39]. The graphene nanopowder (30-50 sheets/monolayers per aggregate) was used rather than traditional single-sheet graphene because it is more cost-effective. Even so, the cost for small quantities of this material corresponds to about $5 for a AA-size alkaline battery. The graphene-based cathode was the best performer in terms of electronic conductivity. The volumetric efficiency of graphene is demonstrated by its doubling the electronic conductivity compared to TIMCAL BNB90, the top performer among the graphites tested. Figure 3.20 shows that the aggregated, but elongated graphene domains provide long, wide highways for electronic conductivity. Furthermore, Figure 3.20b shows that the graphene has molded around the EMD particles, providing excellent particle-to-particle contact. In fact, the small-diameter graphene particles appear to have become more interspersed with the smaller EMD particles, effectively creating access roads to the larger graphene highways. Again, the lubricating and thus good-contacting-nature of graphites is exemplified.

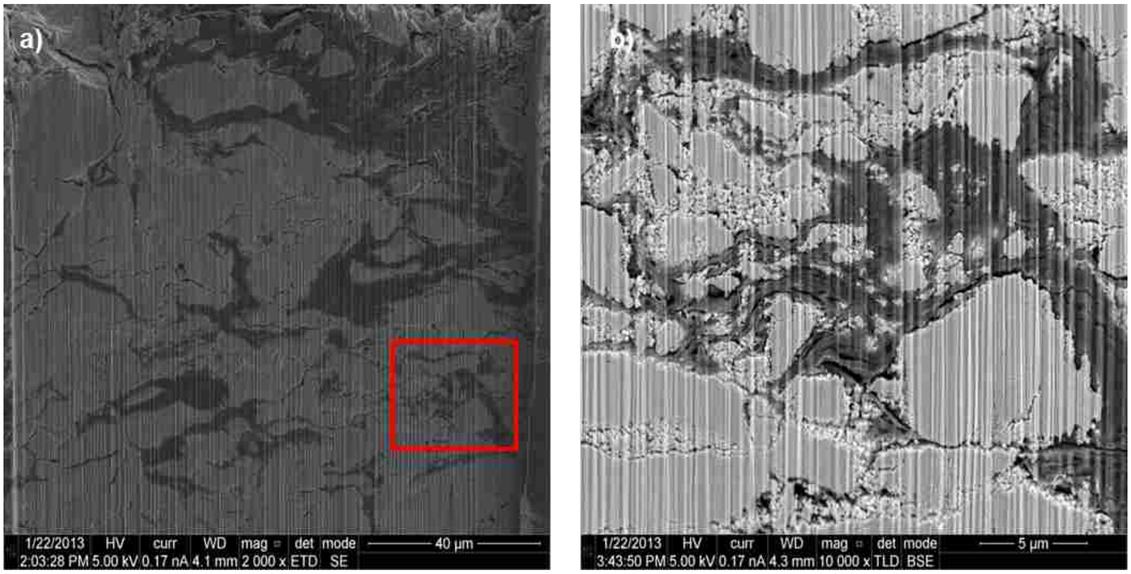

Figure 3.20: SEM/FIB of Graphene Supermarket graphene nanopowder based cathodes, showing the (a) overall microstructure and (b) zoomed-in view. The inter-particle porosity is 13.6% while the overall porosity is 28%.

3.5 Conclusion

Improved understanding of the material-microstructure-transport relationships is an important aspect in improving overall battery performance. This thesis describes research that fills a crucial need to understand the relationships between materials, microstructure, transport processes, and battery performance for primary alkaline battery cathodes. Specifically, the effect of various carbon additives on electronic transport or conductivity within battery cathodes was examined. To accomplish this, a conductivity apparatus was developed and carbon additives with a wide range of physical properties and thus corresponding cathode microstructures were investigated. SEM/FIB imaging was used to investigate the microstructural effects of the various carbon additives. Ultimately, this research provides understanding that paves the way for design and performance improvements for alkaline batteries.

The presence of internal pores within the EMD particles is a significant material and microstructural property that directly affects the ionic conductivity and performance of alkaline battery cathodes. In fact, it nearly doubles the porosity relative to strictly inter-particle porosity. Nevertheless, an ionic conductivity experiment shows that the ionic conductivity is more than 50 times less than the electronic conductivity. This suggests that a typical alkaline battery cathode is disproportionately designed to promote electronic conductivity compared to ionic conductivity. This effect was only cursorily addressed in this work, and additional work is needed to determine how best to optimize ionic and electronic pathways.

Generally, the electronic conductivity increases with decreasing porosity and increasing pressure. Specifically, the electronic conductivity increases with high-aspect-ratio, smaller-particle-diameter, high-surface-area, low-bulk-density or "fluffy" carbon additives as well as more aggregated, but elongated carbon domains with good particle-to-particle contacts.

The smaller-particle-diameter and higher-aspect-ratio carbon additives improve the localized particle-to-particle contacts and longer range connectivities, respectively. High-aspect-ratio carbon additives such as flake graphites (SFG6, MX-15, and BNB90) produce better long-range connectivity, and thus conductivity. This effect is clearly illustrated in the synergy between MX-15 and fiber mixture, which improves conductivity relative to MX-15-based cathodes by 30 and 68% for the compressed and relaxed conditions, respectively. Smaller-particle diameter carbon additives (i.e. SFG6, KS-15) appear more dispersed, providing enhanced long-range, electronically continuous pathways.

The higher-surface-area, low-Scott-density carbon additives (BNB90 and graphene nanopowder) produced more continuous, aggregated carbon domains that provide better conductivity performance compared to extremely dispersed carbon additives (SFG6 and KS-15). In fact, the carbon additives with the highest surface areas and lowest Scott densities provided the two highest electronic conductivities. This reinforces the understanding that conductivity is controlled by both the distance between carbon particles (dispersion) along with the number of particle-to-particle contacts. Furthermore, graphite's lubricating nature is enhanced with lower-bulk-density carbon additives that supply more compressible volume to mold around the larger EMD particles as the sample is compressed, thus producing better particle-to-particle contacting.

This is clearly illustrated by the graphene nanopowder, the best performing carbon additive investigated. Graphene-based cathodes showed aggregated, but elongated carbon domains providing long, wide highways for electronic conductivity in addition to excellent particle-to-particle contact. This behavior is likely due to the graphene nanopowder having the smallest particle diameter, highest surface area, and one of the lowest Scott densities of the additives investigated.

This work refines the relationships between materials, microstructure, transport processes, and battery performance for primary alkaline battery cathodes. Specifically, the relationships between electronic conductivity, material properties, and cathode microstructures for various carbon additives were investigated. This understanding is fundamental to improving battery performance.

3.6 Future work

This work suggests various avenues for future work. The avenues extend from this work toward the central objective of refining understanding of material and microstructure effects on conductivity.

Specifically, this work illustrates trends in electronic conductivity relative to various material properties such as particle diameter, surface area, and bulk density. Additional work could provide a fractional-factorial experiment to investigate interaction between these key material property. Various other mixtures of graphites with other types of graphites or fibers may also be investigated to elucidate these material property effects.

In terms of the cathode microstructure, this work suggests that both the local particle-to-particle contacts and the long-ranged connectivities of the carbon domains are important to the overall electronic conductivity performance. Thus, a more precise understanding of these microstructural effects are essential. These include quantifying the distribution of carbon connectivity throughout the cathode. In addition, quantifying the apparent volumes of the carbon additive with the cathode at various porosities would enable more precise classification of the volumetric efficiency of the various carbon additives. A more detailed, quantitative analysis of the SEM/FIB images could provide this information.

Additionally, the internal nanoporosity of the EMD and the cathode inter-particle porosity have a distribution of pore sizes and configurations. A more precise understanding of these distributions would enable more localized and precise understanding of their effects on ionic conductivity.

In terms of conductivity measurements, future work could entail performing wet (in the presence of electrolyte) electronic conductivity measurements. These wet conductivity measurements would be more physically realistic to the actual electronic conductivities exhibited in alkaline batteries. Additionally, further ionic conductivity measurements for other carbon additives would provide insight into the effect of various carbon additives on ionic transport.

Finally, microstructure and transport models could be developed to describe and predict the effects of the various carbon additives. These models would enable rapid factorial assessment of the effects of various carbon additive properties and microstructures on electronic and ionic conductivities.

In general, refined understanding of the material-microstructure-transport relationships that are fundamental to battery performance provides insight to improve material selection, cathode design, and ultimately battery performance.

Bibliography

[1] M. S. Whittingham, Chemical Reviews **104**, 4271 (2004), URL `http://dx.doi.org/10.1021/cr020731c`.

[2] B. Scrosati and J. Garche, Journal of Power Sources **195**, 2419 (2010), URL `http://www.sciencedirect.com/science/article/pii/S0378775309020564`.

[3] M. Winter and R. J. Brodd, Chemical Reviews **104**, 4245 (2004), URL `http://dx.doi.org/10.1021/cr020730k`.

[4] D. Chung, in *Carbon Filaments and Nanotubes: Common Origins, Differing Applications*, edited by L. P. Biro, C. A. Bernardo, G. G. Tibbetts, and P. Lambin (Springer Netherlands, 2001), vol. 372 of *NATO ASI Series*, pp. 275–288, ISBN 978-94-010-0777-1, URL `http://dx.doi.org/10.1007/978-94-010-0777-1_20`.

[5] Z. Spitalsky, D. Tasis, K. Papagelis, and C. Galiotis, Progress in Polymer Science **35**, 357 (2010), ISSN 0079-6700, URL `http://www.sciencedirect.com/science/article/pii/S0079670009000859`.

[6] Y. Wang, J. Wu, and F. Wei, Carbon **41**, 2939 (2003), ISSN 0008-6223, URL `http://www.sciencedirect.com/science/article/pii/S0008622303003907`.

[7] K. Kinoshita, *Carbon: Electrochemical and physicochemical properties* (Wiley, 1988).

[8] M. Wissler, Journal of Power Sources **156**, 142 (2006), ISSN 0378-7753, URL `http://www.sciencedirect.com/science/article/pii/S0378775306003430`.

[9] D. Chung, Journal of Materials Science **37**, 1475 (2002), ISSN 0022-2461, URL `http://dx.doi.org/10.1023/A:1014915307738`.

[10] W. Lu and D. Chung, Carbon **40**, 447 (2002), ISSN 0008-6223, URL `http://www.sciencedirect.com/science/article/pii/S0008622301002330`.

[11] D. D. L. Chung, Journal of Materials Science **39**, 2645 (2004), ISSN 0022-2461, URL `http://dx.doi.org/10.1023/B:JMSC.0000021439.18202.ea`.

[12] A. Urfer, G. Lawrance, and D. Swinkels, Journal of Applied Electrochemistry **31**, 341 (2001), ISSN 0021-891X, URL `http://dx.doi.org/10.1023/A:1017512721635`.

[13] W. Guo, Y.-X. Yin, S. Xin, Y.-G. Guo, and L.-J. Wan, Energy & Environmental Science **5**, 5221 (2012), URL `http://dx.doi.org/10.1039/C1EE02148F`.

[14] W. Guo, J. Su, Y.-H. Li, L.-J. Wan, and Y.-G. Guo, Electrochimica Acta **72**, 81 (2012), URL `http://www.sciencedirect.com/science/article/pii/S0013468612005282`.

[15] J.-Y. Huot, in *24th International Battery Seminar & Exhibit* (2007), URL `http://www.timcal.com/Scopi/Group/Timcal/timcal.nsf/pagesref/MCOA-7S6K83/$File/Poster_Roles_of_Carbon_in_Modern_Power_Sources.pdf`.

[16] D. Simon, R. Morton, and J. Gislason, International Center for Diffraction Data 2004, Advances in X-ray Analysis **47**, 267 (2004), http://www.icdd.com/resources/axa/vol47/V47_38.pdf.

[17] D. E. Stephenson, Ph.D. thesis, Brigham Young University (2011).

[18] S. Kuroda, N. Tobori, M. Sakuraba, and Y. Sato, Journal of Power Sources **119-121**, 924 (2003), ISSN 0378-7753, URL `http://www.sciencedirect.com/science/article/pii/S0378775303002301`.

[19] J. K. Hong, J. H. Lee, and S. M. Oh, Journal of Power Sources **111**, 90 (2002), ISSN 0378-7753, URL `http://www.sciencedirect.com/science/article/pii/S0378775302002641`.

[20] S. Mandal, J. M. Amarilla, J. Ibez, and J. M. Rojo, Journal of The Electrochemical Society **148**, A24 (2001), `http://jes.ecsdl.org/content/148/1/A24.full.pdf+html`, URL `http://jes.ecsdl.org/content/148/1/A24.abstract`.

[21] J. Xu, J. P. Donohoe, and C. U. P. Jr., Composites Part A: Applied Science and Manufacturing **35**, 693 (2004), ISSN 1359-835X, URL `http://www.sciencedirect.com/science/article/pii/S1359835X04000478`.

[22] G. Chen, W. Weng, D. Wu, and C. Wu, European Polymer Journal **39**, 2329 (2003), ISSN 0014-3057, URL `http://www.sciencedirect.com/science/article/pii/S0014305703001915`.

[23] J. J.S. Andrade, A. Auto, Y. Kobayashi, Y. Shibusa, and K. Shirane, Physica A: Statistical Mechanics and its Applications **248**, 227 (1998), ISSN 0378-4371, URL `http://www.sciencedirect.com/science/article/pii/S0378437197005682`.

[24] Y.-B. Yi and A. M. Sastry, Proceedings of the Royal Society of London. Series A: Mathematical, Physical and Engineering Sciences **460**, 2353 (2004), `http://rspa.royalsocietypublishing.org/content/460/2048/2353.full.pdf+html`, URL `http://rspa.royalsocietypublishing.org/content/460/2048/2353.abstract`.

[25] G. G. Tibbetts, M. L. Lake, K. L. Strong, and B. P. Rice, Composites Science and Technology **67**, 1709 (2007), ISSN 0266-3538, URL `http://www.sciencedirect.com/science/article/pii/S0266353806002338`.

[26] K.-J. Euler, Journal of Power Sources **3**, 117 (1978), ISSN 0378-7753, URL `http://www.sciencedirect.com/science/article/pii/0378775378800111`.

[27] G. Wang, Z. Shao, and Z. Yu, Nanotechnology **18**, 205705 (2007).

[28] Q. Lin and J. N. Harb, Journal of The Electrochemical Society **151**, A1115 (2004), `http://jes.ecsdl.org/content/151/8/A1115.full.pdf+html`, URL `http://jes.ecsdl.org/content/151/8/A1115.abstract`.

[29] T. Takamura and R. J. Brodd, in *New Carbon Based Materials for Electrochemical Energy Storage Systems: Batteries, Supercapacitors and Fuel Cells*, edited by I. V. Barsukov, C. S. Johnson, J. E. Doninger, and V. Z. Barsukov (Springer Netherlands, 2006), vol. 229 of *NATO Science Series*, pp. 157–169, ISBN 978-1-4020-4812-8, URL `http://dx.doi.org/10.1007/1-4020-4812-2_12`.

[30] M. Dohzono, H. Katsuki, and M. Egashira, Journal of The Electrochemical Society **136**, 1255 (1989), `http://jes.ecsdl.org/content/136/5/1255.full.pdf+html`, URL `http://jes.ecsdl.org/content/136/5/1255.abstract`.

[31] W. Guoping, Z. Qingtang, Y. Zuolong, and Q. MeiZheng, Solid State Ionics **179**, 263 (2008), ISSN 0167-2738, URL `http://www.sciencedirect.com/science/article/pii/S0167273808000271`.

[32] I. V. Thorat, V. Mathur, J. N. Harb, and D. R. Wheeler, Journal of Power Sources **162**, 673 (2006), ISSN 0378-7753, URL `http://www.sciencedirect.com/science/article/pii/S0378775306011918`.

[33] K. Striebel, A. Sierra, J. Shim, C.-W. Wang, and A. Sastry, Journal of Power Sources **134**, 241 (2004), ISSN 0378-7753, URL `http://www.sciencedirect.com/science/article/pii/S0378775304004677`.

[34] B. Jin, H.-B. Gu, W. Zhang, K.-H. Park, and G. Sun, Journal of Solid State Electrochemistry **12**, 1549 (2008), ISSN 1432-8488, URL `http://dx.doi.org/10.1007/s10008-008-0509-3`.

[35] C. A. Frysz, X. Shui, and D. Chung, Journal of Power Sources **58**, 41 (1996), ISSN 0378-7753, URL `http://www.sciencedirect.com/science/article/pii/0378775395022910`.

[36] J. K. Hong, J. H. Lee, and S. M. Oh, Journal of Power Sources **111**, 90 (2002), ISSN 0378-7753, URL `http://www.sciencedirect.com/science/article/pii/S0378775302002641`.

[37] Z. Bakenov and I. Taniguchi, Journal of Power Sources **195**, 7445 (2010), ISSN 0378-7753, URL `http://www.sciencedirect.com/science/article/pii/S0378775310008487`.

[38] D. H. Jang and S. M. Oh, Electrochimica Acta **43**, 1023 (1998), ISSN 0013-4686, URL `http://www.sciencedirect.com/science/article/pii/S001346869700265X`.

[39] P. Guo, H. Song, X. Chen, L. Ma, G. Wang, and F. Wang, Analytica Chimica Acta **688**, 146 (2011), ISSN 0003-2670, URL `http://www.sciencedirect.com/science/article/pii/S0003267011000547`.

[40] J. Shim and K. A. Striebel, Journal of Power Sources **119-121**, 955 (2003), ISSN 0378-7753, URL `http://www.sciencedirect.com/science/article/pii/S0378775303002970`.

[41] R. Morris, B. G. Dixon, T. Gennett, R. Raffaelle, and M. J. Heben, Journal of Power Sources **138**, 277 (2004), ISSN 0378-7753, URL `http://www.sciencedirect.com/science/article/pii/S037877530400669X`.

[42] G. Wang, J. ho Ahn, J. Yao, M. Lindsay, H. Liu, and S. Dou, Journal of Power Sources **119-121**, 16 (2003), ISSN 0378-7753, URL `http://www.sciencedirect.com/science/article/pii/S0378775303001174`.

[43] J. Gnanaraj, Y. S. Cohen, M. Levi, and D. Aurbach, Journal of Electroanalytical Chemistry **516**, 89 (2001), ISSN 1572-6657, URL `http://www.sciencedirect.com/science/article/pii/S0022072801006635`.

[44] P. Johns, M. Roberts, and J. Owen, J. Mater. Chem. **21**, 10153 (2011), ISSN 0959-9428, URL `http://dx.doi.org/10.1039/C0JM04357E`.

[45] F.-Y. Su, C. You, Y.-B. He, W. Lv, W. Cui, F. Jin, B. Li, Q.-H. Yang, and F. Kang, J. Mater. Chem. **20**, 9644 (2010), ISSN 0959-9428, URL `http://dx.doi.org/10.1039/C0JM01633K`.

[46] M. Endo, Y. Kim, T. Hayashi, K. Nishimura, T. Matusita, K. Miyashita, and M. Dresselhaus, Carbon **39**, 1287 (2001), ISSN 0008-6223, URL `http://www.sciencedirect.com/science/article/pii/S0008622300002955`.

[47] F.-Y. Su, Y.-B. He, B. Li, X.-C. Chen, C.-H. You, W. Wei, W. Lv, Q.-H. Yang, and F. Kang, Nano Energy **1**, 429 (2012), ISSN 2211-2855, URL `http://www.sciencedirect.com/science/article/pii/S2211285512000705`.

[48] K. Euler, Mat. Chem. **7**, 291 (1982).

[49] S. W. Donne and J. H. Kennedy, J. Applied Electrochem. **34**, 159 (2004).

[50] P. Ruetschi and R. Giovanoli, Journal of The Electrochemical Society **135**, 2663 (1988), `http://jes.ecsdl.org/content/135/11/2663.full.pdf+html`, URL `http://jes.ecsdl.org/content/135/11/2663.abstract`.

[51] E. Sezer, in *The New Froniter of Organic and Composite Nanotechnology* (Elsevier, 2008).

[52] D. D. L. Chung, Journal of Materials Science **22**, 4190 (1987), ISSN 0022-2461, URL `http://dx.doi.org/10.1007/BF01132008`.

[53] T.-T. Lim and X. Huang, Chemosphere **66**, 955 (2007), ISSN 0045-6535, URL `http://www.sciencedirect.com/science/article/pii/S0045653506007235`.

[54] M. Toyoda and M. Inagaki, **38**, 199 (2000), ISSN 0008-6223, URL `http://ac.els-cdn.com/S0008622399001748/1-s2.0-S0008622399001748-main.pdf?_tid=91acc4aa8c84db9ec61e4db6ca437d44&acdnat=1344989706_cfefb28056ec9077ee7ba3a322b9979d`.

[55] *Carbon Powder-Based Solutions for Alkaline Batteries* (TIMCAL, 2011), URL `http://www.timcal.com/scopi/group/timcal/timcal.nsf/pagesref/MCOA-7S6JFG/$File/TIMCAL_brochure_alkaline.pdf`.

[56] *Graphene supermarket. "graphene nanopowder: 12 nm flakes-5 g"*, `https://graphene-supermarket.com/Graphene-Nanopowder-12-nm-Flakes-5-g.html` (2013), accessed May 9, 2013.

[57] *Pyrograf products, inc. "pyrograf(c)-iii carbon nanofiber"*, `http://pyrografproducts.com/Merchant5/merchant.mvc?Screen=cp_nanofiber` (2013), accessed May 9, 2013.

[58] E. Abram, D. Sinclair, and A. West, Journal of Electroceramics **7**, 179 (2001), ISSN 1385-3449, URL `http://dx.doi.org/10.1023/A%3A1014435112280`.

[59] B. C. Reed, American Journal of Physics **57**, 642 (1989), URL `http://link.aip.org/link/?AJP/57/642/1`.

[60] G. Mesri and T. Hayat, Canadian Geotechnical Journal **30**, 647 (1993), `http://www.nrcresearchpress.com/doi/pdf/10.1139/t93-056`, URL `http://www.nrcresearchpress.com/doi/abs/10.1139/t93-056`.

[61] N. R. Draper and H. Smith, *Applied Regression Analysis (Wiley Series in Probability and Statistics)* (John Wiley & Sons, Inc., 1998), 3rd ed.

[62] I. V. Thorat, D. E. Stephenson, N. A. Zacharias, K. Zaghib, J. N. Harb, and D. R. Wheeler, Journal of Power Sources **188**, 592 (2009), ISSN 0378-7753, URL `http://www.sciencedirect.com/science/article/pii/S0378775308023574`.

[63] R. Gilliam, J. Graydon, D. Kirk, and S. Thorpe, International Journal of Hydrogen Energy **32**, 359 (2007), ISSN 0360-3199, <ce:title>Fuel Cells</ce:title>, URL `http://www.sciencedirect.com/science/article/pii/S0360319906005428`.

[64] *Improved manganese dioxide for alkaline cells* (2009), URL `http://www.google.com/patents/EP1490918B1?cl=en`.

[65] *Electrolytic manganese dioxide*, `http://www.tronox.com/products/electrolytic-manganese-dioxide/` (2013), accessed May 9, 2013.

[66] E. Presiler, J. Applied Electrochem. **6**, 311 (1976).